Biomimetic Intelligence and Robotics 5 (2025) 100234

Contents lists available at ScienceDirect

Biomimetic Intelligence and Robotics

journal homepage: www.elsevier.com/locate/birob

Research Article

Tendon friction compensation and slack avoidance for trajectory tracking control of the tendon-driven medical continuum manipulator

Pengyu Du [a,1], Jianxiong Hao [a,1], Kun Qian [b], Yue Zhang [c], Zhiqiang Zhang [c,*], Chaoyang Shi [a,*]

[a] School of Mechanical Engineering, Tianjin University, Tianjin 300072, China
[b] School of Engineering and Physical Sciences, Heriot-Watt University, Edinburgh EH14 4AS, UK
[c] School of Electronic and Electrical Engineering, University of Leeds, Leeds LS2 9JT, UK

ARTICLE INFO

Article history:
Received 11 February 2025
Revised 20 March 2025
Accepted 9 April 2025
Available online 23 April 2025

Keywords:
Continuum manipulator
Minimally invasive surgeries
Trajectory tracking
Adaptive fuzzy control

ABSTRACT

Tendon-driven continuum manipulators can perform tasks in confined environments due to their flexibility and curvilinearity, especially in minimally invasive surgeries. However, the friction along tendons and tendon slack present challenges to their motion control. This work proposes a trajectory tracking controller based on adaptive fuzzy sliding mode control (AFSMC) for the tendon-driven continuum manipulators. It consists of a sliding mode control (SMC) law with two groups of adaptive fuzzy subcontrollers. The first one is utilized to estimate and compensate for friction forces along tendons. The second one adapts the switching terms of SMC to alleviate the chattering phenomenon and enhance control robustness. To prevent tendon slack, an antagonistic strategy along with the AFSMC controller is adopted to allocate driving forces. Simulation and experiment studies have been conducted to investigate the efficacy of the proposed controller. In free space experiments, the AFSMC controller generates an average root-mean-square error (RMSE) of 0.42% compared with 0.90% of the SMC controller. In the case of a 50 g load, the proposed controller reduces the average RMSE to 1.47% compared with 4.29% of the SMC controller. These experimental results demonstrate that the proposed AFSMC controller has high control accuracy, robustness, and reduced chattering.

1. Introduction

Continuum manipulators can continuously deform due to their flexibility, thus suitable for operating in unstructured and confined environments. In minimally invasive medical interventions, their curvilinearity enables them to traverse through tortuous surgical corridors, and their pliability enhances safety during operations [1]. Hence, they have diverse applications across different medical fields [2–5], including flexible endoscopy, single-port surgery, transluminal surgery, and so on. These surgical procedures mainly involve two stages: approaching/accessing target tissues and tissue manipulation, as illustrated in Fig. 1. Among various actuation types, the tendon-driven design emerges as the predominantly favored choice for continuum manipulators, evident not only in commercial products (e.g., da Vinci SP® system and Monarch® platform) but also in research [6–8]. To achieve both efficiency and safety in surgeries, it is imperative to maintain precise control over dynamic trajectories, especially for the approach stage. However, the infinite-dimensional state space and strong nonlinearity and uncertainty in material flexure intrinsic to the continuum manipulators present challenges for their motion control [4,9]. To overcome these challenges, various control methods have been proposed, categorized as position control or trajectory control based on their corresponding modeling approaches [4].

Position control moves continuum manipulators in a quasi-static way, relying on kinematic or static models. The typical kinematics derived from the constant curvature (CC) assumption [10] represents the continuum manipulator's shape as circular arcs with finite parameters. Based on this kinematic model, either inverse/pseudoinverse of Jacobians [11–13] or analytical inversion [14,15] can facilitate the implementation of position control. However, the CC assumption may exhibit large deviations in the presence of external loading or disturbances. Therefore, position control approaches based on statics that utilize the principle of continuum mechanics [16,17] have higher precision in these situations. However, these statics-based control approaches involve complex and high-dimensional formulations in their solving process. Overall, the above position control approaches assume that the manipulator is under quasi-static equilibrium, and thus may face challenges in achieving accurate tracking of trajectories with higher speeds.

---

* Corresponding authors.
E-mail addresses: Z.Zhang3@leeds.ac.uk (Z. Zhang), chaoyang.shi@tju.edu.cn (C. Shi).

[1] The two authors contributed equally to this work.

https://doi.org/10.1016/j.birob.2025.100234

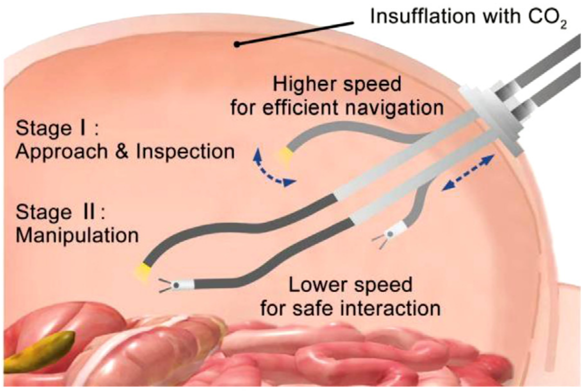

Fig. 1. Surgical procedures divided into two main stages based on performed operations. Stage I (Approach stage): the surgeon inspects the surrounding tissues and navigates to the target site with higher speed for efficient access and screening. Stage II (Manipulation stage): the surgeon performs specific manipulations with lower speed for safe tissue interaction.

In contrast, trajectory control is vital to efficient navigation in surgeries as illustrated in Fig. 1, which typically relies on dynamic modeling. For computational efficiency, common control-oriented dynamic models are derived based on CC assumption and principles of dynamics such as the Lagrange equation. Moreover, under the dynamic modeling framework, existing control theories for dynamic systems can be applied to continuum manipulators, such as feedback linearization plus PD control [18–20]. Moreover, the PID controller can be integrated with fuzzy logic control [21] to dynamically tune its parameters with enhanced robustness. However, this fuzzy controller typically requires empirical design and lacks adaptability when external disturbances change. Because there are always modeling simplifications and external disturbances, robust control methods such as sliding mode control (SMC) are preferred. For example, an SMC controller is designed for an extensible continuum manipulator [22], demonstrating faster error convergence than the PD controller. For enhanced control robustness, an adaptive sliding mode controller is proposed in [23], where the adaptive term is utilized to estimate the unknown model parameters and the upper bound of external disturbances. Besides, the SMC can also be combined with the disturbance observer [24], which can compensate for system uncertainties. Moreover, it utilizes the boundary layer technique to overcome the chattering phenomenon inherent in SMC. It should be noted that most existing trajectory control methods are designed for continuum manipulators driven by pneumatic muscles. This form of actuation can generate bidirectional driving forces with fast response speed, and it actuates the manipulator with high force transmission efficiency [25,26]. Thus, it is convenient to implement trajectory controllers whose outputs are driving forces to these manipulators. Nevertheless, pneumatic actuation typically results in larger robot sizes, limiting its applicability in medical fields [4,9].

Considering trajectory control of tendon-driven continuum manipulators, extra challenges emerge. Firstly, internal friction along tendons induces a loss of driving force and deterioration in motion control accuracy [27]. Efforts have been made toward modeling, such as the utilization of the Dahl friction model [28] or the Capstan equation [29–31] to predict the distributed friction forces. However, their accuracy is limited by modeling simplifications and elaborate experiments are demanded to identify the friction parameters. In contrast, model-free methods such as the support vector machine [32] can be applied to estimate friction forces. However, it requires intricate processes to collect sample data for offline training. Secondly, tendons are incapable of supporting compressive driving forces, which can lead to slack issues during operation. Slackened tendons result in actuation backlash and may fail to actuate the manipulator. The most direct and efficient solution is to ensure that the tendons are actuated by tensile forces. For instance, an optimization algorithm is designed in [33] to solve for the inverse kinematics. The constraints on tendon driving forces and static relationships ensure that all tendons are kept under tension. Similarly, based on statics and linear distributions of tendon tensions, a slack avoidance algorithm is proposed in [34], which prevents tendon slack by limiting the length of the manipulator. Nevertheless, existing solutions to tendon slack are based on static analysis, thus not applicable to trajectory control scenarios. Due to these two challenges, few studies have been conducted on the trajectory control of tendon-driven continuum manipulators based on dynamic modeling so far.

To address the above limitations, a trajectory controller based on adaptive fuzzy sliding mode control (AFSMC) is proposed for the tendon-driven continuum manipulator. The controller is built upon a dynamic model derived from CC kinematics utilizing the Lagrange equation, providing computational efficiency for real-time trajectory control. The proposed AFSMC controller consists of an SMC law and two independent groups of adaptive fuzzy subcontrollers. The first one is designed to estimate and compensate for friction forces along tendons. The second one adapts the traditional switching terms of the SMC with fuzzy switching terms to alleviate the chattering phenomenon and enhance robustness. To prevent tendon slack, an antagonistic strategy is developed for allocating the driving forces generated by the AFSMC controller. The friction estimation is designed based on tendon friction's physical characteristics, and the fuzzy switching terms do not require prior knowledge of disturbance bounds due to their adaptive law design. Simulation and experimental studies are conducted to illustrate the efficacy of the proposed method. With these friction compensation and fuzzy switching terms, the AFSMC controller demonstrates higher tracking accuracy and better control robustness against external disturbance.

2. Materials and methods

2.1. Hardware configuration of the continuum robot system

The overall hardware configuration of the robotic system mainly includes a tendon-driven continuum manipulator unit, a binocular vision measurement unit, and a control unit, as illustrated in Fig. 2. A standard spacing disk-type continuum manipulator with a nitinol central backbone has been utilized for experimental validation of the proposed control method. This manipulator is driven by two pairs of antagonistic tendons connected to linear modules. Each linear module is constructed with dual lateral guide rails and a central lead screw to convert the rotation of a DC motor (Maxon, DCX-19X, Switzerland) to linear motion. The motors are equipped with optical encoders (Maxon, ENX16) to detect the motions of tendons, and the linear modules are integrated with force sensors (JinNuo, JLBS-MD, China) to measure the tendons' driving forces. The amplifiers (MotionG, UF-48V10AEDR, China) can actuate the DC motors to generate the target driving forces of the tendons, with a working principle similar to [35]. The binocular vision measurement unit (NDI Polaris, Canada) detects the distal tip position of the continuum manipulator with the optical marker attached at its distal tip. The measured position is sent to the host computer (Core i7 processor @ 2.20 GHz, 16-GB RAM) as feedback on position through a USB connection. The embedded controller (CX-5140, Beckhoff, Germany) receives control signals from the host computer through a TCP/IP connection and relays these commands to the amplifiers via EtherCAT. Meanwhile, the amplifiers read data from encoders and send feedback on tendon lengths and velocities to the host computer through the embedded controller.

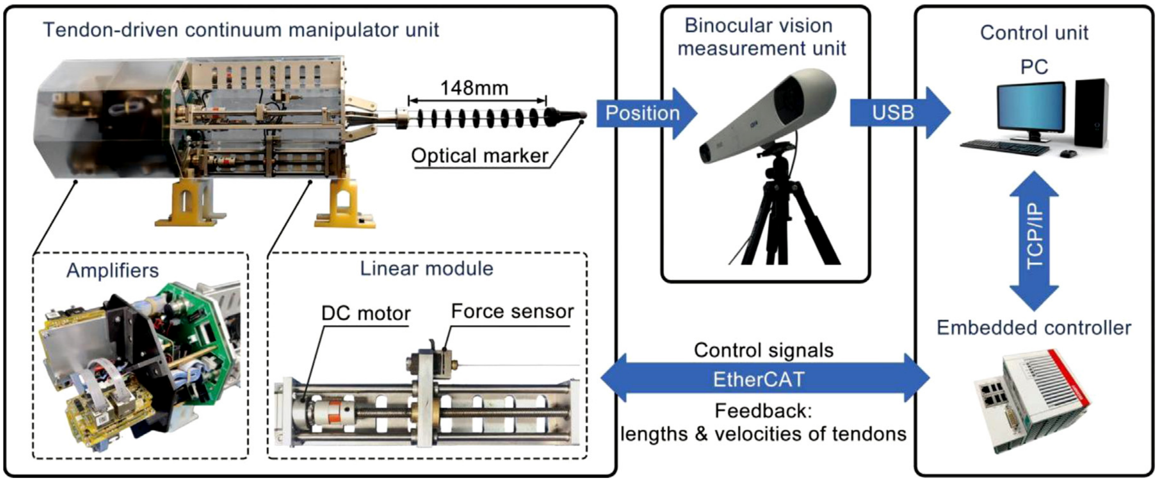

Fig. 2. Hardware configuration of the continuum robot system.

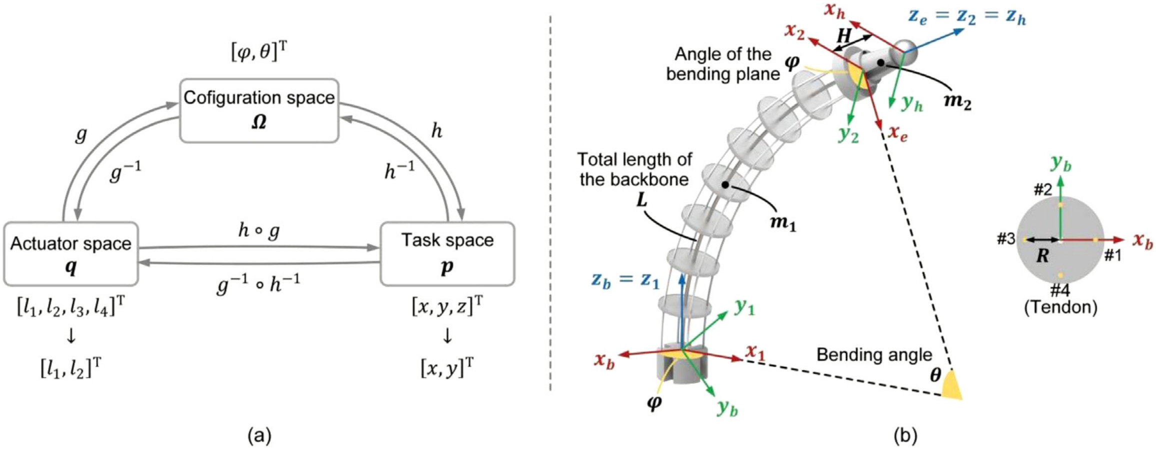

Fig. 3. The kinematics of the continuum manipulator based on the CC assumption. (a) The mapping relationships between different spaces. (b) The frames and parameters defined for the continuum manipulator.
Notes: m_1 and m_2 separately denote the mass of the manipulator arm and end effector. Their positions are formulated respect to frames *1 and *2. Meanwhile, *b, *e, and *h denote the base, end, and head frame, respectively.

2.2. Kinematic and dynamic modeling of the tendon-driven continuum manipulator

The constant curvature (CC) is a well-suited characteristic for continuum manipulators and represents the manipulator's configuration with finite generalized coordinates. Based on CC kinematics, the kinetic and potential energy can be formulated via the generalized coordinates, and the Lagrange equation can be further applied to derive the dynamic model.

2.2.1. Kinematic modeling based on the CC assumption

Different spaces are defined to facilitate the representation of the continuum manipulator's states under the CC assumption (Fig. 3(a)). The actuator space contains the lengths of tendons: $\boldsymbol{q} = [l_1, l_2, l_3, l_4]^{\mathrm{T}}$, where l_i $(i = 1, 2, 3, 4)$ denotes the length of the ith tendon. The configuration space contains parameters $\boldsymbol{\Omega} = [\varphi, \theta]^{\mathrm{T}}$ to describe the bending motion, where φ is the angle of the bending plane and θ represents the bending angle (Fig. 3(b)). The task space contains the position of the end effector: $\boldsymbol{p} = [x, y, z]^{\mathrm{T}}$. Kinematics involves establishing mappings g and h between these spaces.

The mapping g can be formulated as Eq. (1), where L is the length of the central backbone, R denotes the radius of the manipulator (Fig. 3(b)). The tendon displacements are equal and opposite for each antagonistic pair (l_1, l_3) and (l_2, l_4) under the assumption that the central backbone is incompressible. Therefore, the actuator space can be simplified as $\boldsymbol{q} = [l_1, l_2]^{\mathrm{T}}$.

$$\boldsymbol{\Omega} = g(\boldsymbol{q}) = \begin{bmatrix} \arctan\left(\dfrac{L-l_2}{L-l_1}\right) \\ \frac{\sqrt{(L-l_2)^2+(L-l_1)^2}}{R} \end{bmatrix} \tag{1}$$

To derive the mapping h, a set of frames is defined as illustrated in Fig. 3(b). Multiplying the series of transformations between those frames, the mapping h is represented as Eq. (2), where H denotes the height of the end effector. This paper focuses on investigating the x and y coordinates because the value of coordinate z can be decided by the value of x and y. Therefore, the task space is simplified to $\boldsymbol{p} = [x, y]^{\mathrm{T}}$.

$$\boldsymbol{p} = h(\boldsymbol{\Omega}) = \begin{bmatrix} H\cos\varphi\sin\theta + \frac{L\cos\varphi(1-\cos\theta)}{\theta} \\ H\sin\varphi\sin\theta + \frac{L\sin\varphi(1-\cos\theta)}{\theta} \end{bmatrix} \tag{2}$$

As a result, forward kinematics can be represented as the composition of the mapping g and h: $\boldsymbol{p} = h \circ g(\boldsymbol{q})$. Differentiating the equation of forward kinematics, the Jacobian matrix $\boldsymbol{J}$ can be obtained by Eq. (3), whose inverse can be applied for differential inverse kinematics.

$$\dot{\boldsymbol{p}} = \tfrac{\partial h}{\partial \boldsymbol{\Omega}} \tfrac{\partial g}{\partial \boldsymbol{q}} \dot{\boldsymbol{q}} = \boldsymbol{J}\dot{\boldsymbol{q}} \tag{3}$$

2.2.2. Dynamic modeling based on the Lagrange equation

To develop a control-oriented dynamic model, the continuous mass distribution is simplified to discrete points, enhancing both modeling and computational efficiency [36]. Similar to the hypothesis in [20,37], the distributed mass of the manipulator arm is centralized to its midpoint. Another mass point located at the distal tip is also utilized to account for the mass of the end effector. The mass of these two discrete points is separately denoted by m_1 and m_2 as shown in Fig. 3(b).

The Lagrange equation can be written as Eq. (4), where T and U respectively denote the kinetic and potential energy of the continuum manipulator, $\boldsymbol{q}$ serves as the generalized coordinates, and $\boldsymbol{Q}$ represents the generalized forces.

$$\frac{d}{dt}\frac{\partial T}{\partial \dot{\boldsymbol{q}}} - \frac{\partial T}{\partial \boldsymbol{q}} + \frac{\partial U}{\partial \boldsymbol{q}} = \boldsymbol{Q} \tag{4}$$

As indicated by Eq. (4), the derivation of the dynamic model is divided into three parts: kinetic energy T, potential energy U, and generalized forces $\boldsymbol{Q}$.

Under the assumption of centralized mass distribution, the kinetic energy T can be represented as:

$$T = \frac{1}{2}\sum_{i=1}^{2} m_i \boldsymbol{v}_{ci}^{\mathrm{T}} \boldsymbol{v}_{ci} \tag{5}$$

where $\boldsymbol{v}_{ci} \in \mathbb{R}^3$ is the velocity of mass m_i. The contribution of the rotational energy to the kinetic energy can be omitted compared with the translational energy [38]. Based on the CC kinematics, $\boldsymbol{v}_{ci}$ can be expressed as the derivative of the position $\boldsymbol{p}_{ci}$ of mass m_i.

$$\begin{bmatrix} \boldsymbol{v}_{ci} \\ 0 \end{bmatrix} = \frac{d}{dt}\begin{bmatrix} \boldsymbol{p}_{ci} \\ 1 \end{bmatrix} = \dot{\boldsymbol{T}}_i^b \begin{bmatrix} \boldsymbol{p}_{c_i}^i \\ 1 \end{bmatrix} + \boldsymbol{T}_i^b \begin{bmatrix} \dot{\boldsymbol{p}}_{c_i}^i \\ 0 \end{bmatrix} \tag{6}$$

where $\boldsymbol{T}_i^b$ denotes the transformation matrix from $\boldsymbol{O}_i\{x_i y_i z_i\}$ $(i = 1, 2)$ to $\boldsymbol{O}_b$, and the position $\boldsymbol{p}_{c_i}^i$ is formulated relative to the frame $\boldsymbol{O}_i$ (i.e., $\boldsymbol{p}_{c_1}^1 = \left[\frac{L}{\theta}\cos\varphi\left(1-\cos\frac{\theta}{2}\right), \frac{L}{\theta}\sin\varphi\left(1-\cos\frac{\theta}{2}\right), \frac{L}{\theta}\sin\frac{\theta}{2}\right]^{\mathrm{T}}$, $\boldsymbol{p}_{c_2}^2 = \left[0, 0, \frac{H}{2}\right]^{\mathrm{T}}$). The kinetic energy can be obtained by substituting the velocities $\boldsymbol{v}_{ci}$ into Eq. (5).

The potential energy U includes the gravitational potential energy U_g of the manipulator and the elastic potential energy U_e of the central backbone. U_g can be formulated as:

$$U_g = -\sum_{i=1}^{2} m_i \boldsymbol{G}^{\mathrm{T}} \boldsymbol{p}_{ci}^b \tag{7}$$

where $\boldsymbol{G}$ denotes the gravitational acceleration vector (equal to $\left[0, -9.8\ \mathrm{m/s^2}, 0\right]^{\mathrm{T}}$ based on the experimental configuration). The elastic energy U_e can be formulated as Eq. (8), where E and I respectively denote the Young's modulus and cross-sectional inertia of the central backbone, and $M(x) = EI\frac{\theta}{L}$ represents the moment along the length of the central backbone.

$$U_e = \int_0^L \frac{M^2}{2EI} dx = \frac{EI}{2L}\theta^2 \tag{8}$$

The generalized forces can be represented by the forces exerted on tendons: $\boldsymbol{Q} = \boldsymbol{F}_d - \boldsymbol{f}$, where $\boldsymbol{F}_d = \left[F_{d1}, F_{d2}\right]^{\mathrm{T}}$ denotes the driving forces, and $\boldsymbol{f} = \left[f_1, f_2\right]^{\mathrm{T}}$ represents the friction forces. However, modeling challenges of friction forces arise from their nonlinearity and uncertainty. To overcome their modeling difficulty, the friction forces are estimated by the adaptive fuzzy subcontrollers, which will be designed in the next section. Based on the above analyses, the derived dynamic model can be written in a compact form:

$$\boldsymbol{M}(\boldsymbol{q})\ddot{\boldsymbol{q}} + \boldsymbol{C}(\boldsymbol{q}, \dot{\boldsymbol{q}})\dot{\boldsymbol{q}} + \boldsymbol{N}(\boldsymbol{q}) + \boldsymbol{f} = \boldsymbol{F}_d \tag{9}$$

where $\boldsymbol{M}(\boldsymbol{q}) \in \mathbb{R}^{2\times 2}$, $\boldsymbol{C}(\boldsymbol{q}, \dot{\boldsymbol{q}}) \in \mathbb{R}^{2\times 2}$, and $\boldsymbol{N}(\boldsymbol{q}) \in \mathbb{R}^{2\times 1}$ are the generalized inertial matrix, Coriolis/centrifugal matrix, and gravity/elastic force vector, respectively.

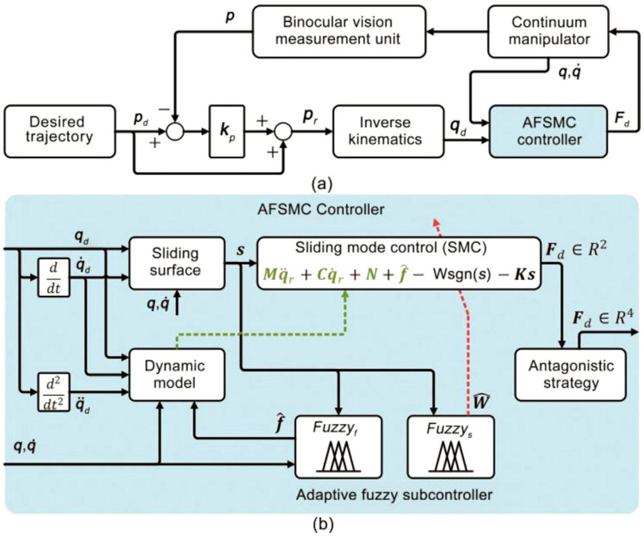

Fig. 4. (a) The workflow of the trajectory tracking control for the tendon-driven continuum manipulator. (b) The details of the proposed AFSMC controller.

2.3. AFSMC controller design of the continuum manipulator

Based on the established dynamic model, the AFSMC controller is proposed in this section to achieve accurate and robust trajectory control of the tendon-driven continuum manipulator. The workflow of the trajectory tracking with this proposed controller is shown in Fig. 4(a). Because the dynamic model is derived in the actuator space, the desired trajectory in the task space $\boldsymbol{p}_d$ should be converted to $\boldsymbol{q}_d$ in actuator space. This conversion is carried out via the inverse kinematics, utilizing the inverse of the Jacobian as defined in Eq. (3). Given the existence of internal friction and external disturbance, the inverse kinematics based on the CC assumption will cause non-negligible errors. Thus, an outer control loop is employed to correct the deviation from the actual inverse kinematics, including both feedforward and proportional feedback action:

$$\boldsymbol{p}_r = \boldsymbol{p}_d + \boldsymbol{k}_p\left(\boldsymbol{p}_d - \boldsymbol{p}\right) \tag{10}$$

where the position feedback $\boldsymbol{p}$ is provided by the binocular vision measurement unit. Upon receiving the desired trajectory $\boldsymbol{q}_d$ together with feedback on tendon lengths $\boldsymbol{q}$ and velocities $\dot{\boldsymbol{q}}$ from motor encoders, the AFSMC controller calculates the driving forces $\boldsymbol{F}_d$ to control the manipulator.

The AFSMC controller mainly includes three components: the SMC law, the antagonistic control strategy, and two groups of adaptive fuzzy subcontrollers, as illustrated in Fig. 4(b). The SMC law serves as the core and fundamental component of the proposed controller, due to its capability to handle nonlinear systems with model uncertainties and external disturbances. With the tracking error in actuator space denoted by $\boldsymbol{e} = \boldsymbol{q} - \boldsymbol{q}_d$, the sliding surface is represented as $\boldsymbol{s} = \boldsymbol{\gamma}\boldsymbol{e} + \dot{\boldsymbol{e}}$, where $\boldsymbol{\gamma}$ is a diagonal positive definite matrix. Then the formulation of the SMC law is derived as:

$$\boldsymbol{F}_d = \boldsymbol{M}\ddot{\boldsymbol{q}}_r + \boldsymbol{C}\dot{\boldsymbol{q}}_r + \boldsymbol{N} - \boldsymbol{W}\mathrm{sgn}(\boldsymbol{s}) - \boldsymbol{K}\boldsymbol{s} \tag{11}$$

where $\boldsymbol{W} = \mathrm{diag}\left(w_1, w_2\right)$, $w_i > 0$ denotes the switching gains and $\boldsymbol{W}\mathrm{sgn}(\boldsymbol{s})$ represents the switching terms. $\boldsymbol{K}$ is a diagonal positive definite matrix, which can accelerate the convergence of errors and enhance stability, and $\dot{\boldsymbol{q}}_r = \dot{\boldsymbol{q}}_d - \boldsymbol{\gamma}\boldsymbol{e}$ is the derivative of the reference trajectory [39] in actuator space.

One problem posed by the tendon-driven approach is the slack of tendons, which occurs when the driving force is thrust

($F_{di} > 0$). Slackened tendons may lead to the failure of actuating the continuum manipulator and the trajectory tracking task. To solve this problem, the AFSMC controller utilizes an antagonistic control strategy, as shown below.

$$\begin{cases} F_{di} = F_{di}, F_{d(i+2)} = 0 & F_{di} \le 0 \\ F_{di} = 0, F_{d(i+2)} = -F_{di} & F_{di} > 0, \end{cases} \quad i \in \{1, 2\} \tag{12}$$

In this strategy, when the calculated driving force of one tendon is thrust, the AFSMC controller converts it to the pulling force of its antagonistic tendon. According to Eq. (12), the driving forces of all tendons will always be pulling forces, thereby preventing tendon slack.

To overcome another problem inherent in the tendon-driven approach, *i.e.*, internal friction along tendons, and to further enhance control performances of SMC, two independent groups of adaptive fuzzy subcontrollers are incorporated. The first group, denoted as $Fuzzy_f$, is designed to estimate the friction forces and compensate them to the dynamic model through a feedforward term. The second group, denoted as $Fuzzy_s$, is utilized to adapt the SMC's traditional switching terms with fuzzy switching terms. Fuzzy control possesses universal approximation capabilities for any real function [40]. Equipped with adaptive laws, it can further approximate unknown functions. The design of these subcontrollers $Fuzzy_f$ and $Fuzzy_s$ is based on the above ability of adaptive fuzzy control, which will be detailed in the following sections.

2.3.1. Estimation of the friction forces along tendons

The friction force along each tendon is governed by various physical factors, including tendon length and velocity, the manipulator's bending angle, and the tendon's driving force [28]. Among these factors, tendon lengths and velocities are the predominant ones, because they directly influence both the manipulator's bending angle and the tendon's driving force. Hence, the subcontrollers $Fuzzy_f$ can effectively approximate the friction force by using the tendon lengths $\boldsymbol{q} = [l_1, l_2]^{\mathrm{T}}$ and velocities $\dot{\boldsymbol{q}} = [\dot{l}_1, \dot{l}_2]^{\mathrm{T}}$ as inputs of the friction estimation. The output of each $Fuzzy_f$ is the estimated friction force $\hat{f}_k$ along tendon #$k (k \in \{1, 2\})$.

To implement fuzzy logic control, it is necessary to specify fuzzy sets for the range of interest of control input and output. For control inputs, suppose $A_i^{a_i} (a_i = 1, 2, \ldots, m)$ and $B_j^{b_j}$ $(b_j = 1, 2, \ldots, n)$ represent fuzzy sets defined for tendon length l_i and tendon velocity $\dot{l}_j$, respectively $(i, j \in \{1, 2\})$. For control output, the fuzzy sets $C_k^{a_1 a_2 b_1 b_2}$ are defined for the estimated friction force $\hat{f}_k$. Then the fuzzy rules can be represented as:

IF l_1 is $A_1^{a_1}$ and l_2 is $A_2^{a_2}$ and $\dot{l}_1$ is $B_1^{b_1}$ and $\dot{l}_2$ is $B_2^{b_2}$ THEN $\hat{f}_k$ is $C_k^{a_1 a_2 b_1 b_2}$

This work utilizes the typical fuzzy controller configuration with singleton fuzzification, product inference, and center-average defuzzification. Based on the above fuzzy rules and controller configuration, the subcontrollers $Fuzzy_f$ can be formulated as:

$$\begin{aligned} \hat{f}_k &= \frac{\sum_{a_1, a_2=1}^{m} \sum_{b_1, b_2=1}^{n} \bar{y}_k^{a_1 a_2 b_1 b_2} \left(\prod_{i=1}^{2} \mu_i^{a_i} (l_i) \prod_{j=1}^{2} \mu_j^{b_j} (\dot{l}_j) \right)}{\sum_{a_1, a_2=1}^{m} \sum_{b_1, b_2=1}^{n} \left(\prod_{i=1}^{2} \mu_i^{a_i} (l_i) \prod_{j=1}^{2} \mu_j^{b_j} (\dot{l}_j) \right)} \\ &= \boldsymbol{\theta}_{f_k}^{T} \boldsymbol{\xi} (\boldsymbol{q}, \dot{\boldsymbol{q}}) , k \in \{1, 2\} \end{aligned} \tag{13}$$

where $\mu_i^{a_i} (\cdot)$ and $\mu_j^{b_j} (\cdot)$ respectively denote the membership functions of $A_i^{a_i}$ and $B_j^{b_j}$. The adjustable parameter $\bar{y}_k^{a_1 a_2 b_1 b_2}$ is the center of the membership function of $C_k^{a_1 a_2 b_1 b_2}$. All the membership functions in this paper are Gaussian membership functions in the form:

$$\mu (x) = \exp \left[-\frac{(x-\rho)^2}{2\sigma^2} \right] \tag{14}$$

As indicated by Eq. (13), the output is a linear combination of fuzzy basis functions [41] in vector $\boldsymbol{\xi} (\boldsymbol{q}, \dot{\boldsymbol{q}}) = [\xi_1 (\boldsymbol{q}, \dot{\boldsymbol{q}}) , \xi_2 (\boldsymbol{q}, \dot{\boldsymbol{q}}) , \ldots , \xi_{m^2 n^2} (\boldsymbol{q}, \dot{\boldsymbol{q}})]^{\mathrm{T}}$ with $\boldsymbol{\theta}_{f_k}$ containing all adjustable coefficients: $\boldsymbol{\theta}_{f_k} = [\bar{y}_k^1, \bar{y}_k^2, \ldots , \bar{y}_k^{m^2 n^2}]^{\mathrm{T}}$. The fuzzy basis function $\xi_{a_1 a_2 b_1 b_2} (\boldsymbol{q}, \dot{\boldsymbol{q}})$, $a_1 a_2 b_1 b_2 \epsilon [1, m^2 n^2]$ can be written as:

$$\frac{\prod_{i=1}^{2} \mu_i^{a_i} (l_i) \prod_{j=1}^{2} \mu_j^{b_j} (\dot{l}_j)}{\sum_{a_1, a_2=1}^{m} \sum_{b_1, b_2=1}^{n} \left(\prod_{i=1}^{2} \mu_i^{a_i} (l_i) \prod_{j=1}^{2} \mu_j^{b_j} (\dot{l}_j) \right)} \tag{15}$$

In experiments, parameters related to membership functions of $\boldsymbol{q}$ and $\dot{\boldsymbol{q}}$ in $\boldsymbol{\xi} (\boldsymbol{q}, \dot{\boldsymbol{q}})$ are set according to the actual range of tendon lengths ($[-6, 6]$ mm) and velocities ($[-15, 15]$ mm/s). The initial value of $\boldsymbol{\theta}_{f_k}$ is randomly assigned and further adjusted by adaptive laws to ensure an accurate approximation of the friction forces. The adaptive laws for $\boldsymbol{\theta}_{f_k}$ are derived based on the Lyapunov synthesis approach as follows, with Γ_k being a positive scalar (details are shown in Appendix A).

$$\dot{\boldsymbol{\theta}}_{f_k} = -\Gamma_k^{-1} s_k \boldsymbol{\xi} (\boldsymbol{q}, \dot{\boldsymbol{q}}) , k \in \{1, 2\} \tag{16}$$

Combining all the estimated friction forces, the feedforward term to compensate for the unknown friction forces can be represented as follows, where $\boldsymbol{\theta}_f = [\boldsymbol{\theta}_{f_1}, \boldsymbol{\theta}_{f_2}]$.

$$\hat{\boldsymbol{f}} \left(\boldsymbol{q}, \dot{\boldsymbol{q}} | \boldsymbol{\theta}_f \right) = \left[\hat{f}_1, \hat{f}_2 \right]^{\mathrm{T}} = \boldsymbol{\theta}_f^{\mathrm{T}} \boldsymbol{\xi} (\boldsymbol{q}, \dot{\boldsymbol{q}}) \tag{17}$$

2.3.2. Design of the fuzzy switching terms

In the SMC law (11), the utilization of function $\operatorname{sgn} (\boldsymbol{s})$ leads to the noncontinuous switching terms $\boldsymbol{W} \operatorname{sgn} (\boldsymbol{s})$ and chattering phenomenon. Moreover, the value of the switching gains $\boldsymbol{W}$ should be assessed in advance according to the boundary of external disturbances, thus the unexpected disturbances will reduce the controller's robustness. To address these limitations, adaptive fuzzy control can be utilized to approximate the desired switching terms $\boldsymbol{W}^* \operatorname{sgn} (\boldsymbol{s})$, where $\boldsymbol{W}^*$ is the upper bound of external disturbances.

Because the desired switching term $W_k^* \operatorname{sgn} (s_k)$, $k \in \{1, 2\}$ is only the function of s_k, the control input of each $Fuzzy_s$ is s_k and the output is the fuzzy switching term $\hat{W}_k$. For control input, suppose $D_k^{t_k} (t_k = 1, 2, \ldots , r)$ are fuzzy sets related to s_k. For control output, suppose $E_k^{t_k} (t_k = 1, 2, \ldots , r)$ are fuzzy sets defined for $\hat{W}_k$. Then the fuzzy rules can be written as:

IF s_k is $D_k^{t_k}$ THEN $\hat{W}_k$ is $E_k^{t_k}$

Based on the above fuzzy rules and the same fuzzy controller configuration as $Fuzzy_f$, the output of the subcontrollers $Fuzzy_s$ can be formulated as:

$$\hat{W}_k = \boldsymbol{\theta}_{W_k}^{\mathrm{T}} \boldsymbol{\xi} (s_k) , k \in \{1, 2\} \tag{18}$$

where $\boldsymbol{\xi} (s_k)$ contains fuzzy basis functions and $\boldsymbol{\theta}_{W_k}$ contains the centers of membership functions of $\hat{W}_k$. In experiments, parameters related to membership functions of s_k in $\boldsymbol{\xi} (s_k)$ can be specified according to the actual range of s_k ($[-0.1, 0.1]$ m) and the initial value of $\boldsymbol{\theta}_{W_k}$ can be set randomly. The adaptive laws of $\boldsymbol{\theta}_{W_k}$ are shown as follows, with ϕ_k being a positive scalar.

$$\dot{\boldsymbol{\theta}}_{W_k} = \phi_k^{-1} s_k \boldsymbol{\xi} (s_k) , k \in \{1, 2\} \tag{19}$$

Therefore, the vector containing all fuzzy switching terms can be written as follows, where $\boldsymbol{\theta}_W = [\boldsymbol{\theta}_{W_1}, \boldsymbol{\theta}_{W_2}]$.

$$\hat{\boldsymbol{W}} (\boldsymbol{s} | \boldsymbol{\theta}_W) = \left[\hat{W}_1, \hat{W}_2 \right]^{\mathrm{T}} = \left[\boldsymbol{\theta}_{W_1}^{\mathrm{T}} \boldsymbol{\xi} (s_1) , \boldsymbol{\theta}_{W_2}^{\mathrm{T}} \boldsymbol{\xi} (s_2) \right]^{\mathrm{T}} \tag{20}$$

It should be noted that the resulting fuzzy switching terms $\hat{\boldsymbol{W}}$ are continuous, which can alleviate the chattering phenomenon. Moreover, it does not require prior knowledge of disturbances,

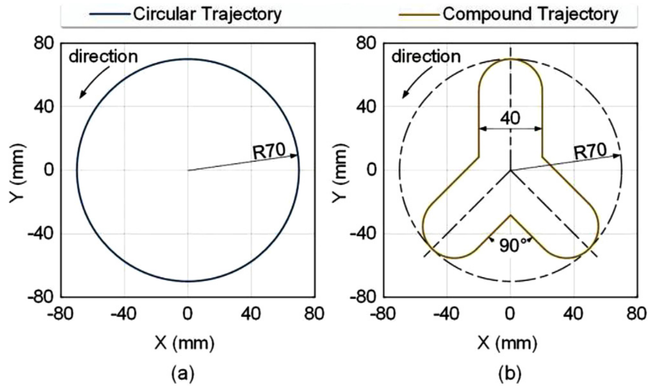

Fig. 5. The desired trajectories utilized in experiments. (a) Circular trajectory. (b) Compound trajectory.

because the adaptive laws (19) can dynamically adjust parameters $\boldsymbol{\theta}_{W_k}$ to ensure approximation to the desired switching terms $\boldsymbol{W}^*\mathrm{sgn}\,(\boldsymbol{s})$. Thus, the fuzzy switching terms $\hat{\boldsymbol{W}}$ can also enhance the controller's robustness.

Merging the estimated friction forces (17) and fuzzy switching terms (20) into Eq. (11), the formulation of the AFSMC controller can be represented as:

$$\boldsymbol{F}_d = \boldsymbol{M}\ddot{\boldsymbol{q}}_{\boldsymbol{r}} + \boldsymbol{C}\dot{\boldsymbol{q}}_{\boldsymbol{r}} + \boldsymbol{N} + \hat{\boldsymbol{f}}\left(\boldsymbol{q}, \dot{\boldsymbol{q}}|\boldsymbol{\theta}_f\right) - \hat{\boldsymbol{W}}\,(\boldsymbol{s}|\boldsymbol{\theta}_W) - \boldsymbol{Ks} \tag{21}$$

The stability proof of this controller and derivation of the adaptive laws (16) and (19) are presented in Appendix A.

3. Experiments and results

3.1. Trajectory tracking experiments for the AFSMC controller in free space

This section implements the proposed AFSMC controller on the physical continuum manipulator for trajectory tracking in free space to investigate its efficacy. To compare with the proposed controller, the traditional SMC controller was utilized as a benchmark with the same control parameters. Two types of 2D trajectories were defined as target motion patterns, as illustrated in Fig. 5. The circular trajectory has a simple shape but can be utilized to test the controllers' ability to track the desired shape, while the compound trajectory changes more dynamically with circular, linear, and angular elements. The tracking time of both trajectories was set as 20 s, thus the resulting speeds were 21.99 mm/s for the circular path and 20.77 mm/s for the compound path.

To assess the tracking performances of these controllers, metrics for quantifying the deviation from the desired trajectories were employed. These metrics include the root-mean-square error (RMSE) between the actual and desired trajectories and the tracking error's standard deviation (SD). The SD can quantify the extent of tracking error's dispersion, thus it can reflect the extent of chattering behaviors as well. Moreover, the shape error (SE) is also defined as Eq. (22) for the circular trajectory. The SE can assess the controllers' ability to track the shape of the desired trajectory.

$$\mathrm{SE} = \sup \left\|\boldsymbol{p} - \boldsymbol{p}_{cen}\right\|_2 - \inf \left\|\boldsymbol{p} - \boldsymbol{p}_{cen}\right\|_2 \tag{22}$$

where $\sup \left\|\boldsymbol{p} - \boldsymbol{p}_{cen}\right\|_2$ and $\inf \left\|\boldsymbol{p} - \boldsymbol{p}_{cen}\right\|_2$ denote the maximal and minimal Euclidean distance between the actual trajectory and its center of the circle, respectively. Moreover, one-tailed Welch's t-tests were conducted to statistically validate the significance of performance improvement of the AFSMC controller. The null hypothesis H_0 and the alternative hypothesis H_1 are defined as follows:

$$H_0: \mu_{AFSMC} = \mu_{SMC}, \quad H_1: \mu_{AFSMC} < \mu_{SMC} \tag{23}$$

where μ_{AFSMC} and μ_{SMC} denote the mean value of the controller errors. The Satterthwaite degrees of freedom is utilized to account for unequal variances between the two controllers. Statistical significance is evaluated at $\alpha = 0.05$ and Cohen's d effect size is calculated to quantify the magnitude of improvement.

Before the actual experiments, simulation studies were performed to qualitatively verify the proposed controller's performances (details are presented in Appendix B). The AFSMC controller demonstrates its feasibility and exhibits high control accuracy with an average RMSE of 0.305 mm on two trajectories (lower than that of the SMC controller by 76.3%). Furthermore, a theoretical friction model with the Dahl friction formulation was also incorporated, and the comparison between the theoretical and estimated friction forces is shown in Fig. 6. The AFSMC controller generates an average FERMSE (friction estimation RMSE) on two trajectories of 0.090N and 0.106N on tendon #1 and tendon #2, respectively. These minor errors confirm the effectiveness of the friction estimation.

For actual experiments, the configurations of the continuum robot system have been illustrated in Fig. 2. The controllers operated at a frequency of 60 Hz, which is limited by the synchronization between different devices (such as amplifiers and the binocular vision measurement unit). All the identified parameters of the physical continuum manipulator and controller parameter settings are enumerated in Table 1. To test the controllers' stability, the trajectories were extended to include two cycles.

The experimental results of trajectory tracking in free space are calculated and listed in Fig. 7 and Table 2. Due to the noncontinuous switching terms, the trajectories generated by the SMC controller exhibit serious chattering behaviors. The fuzzy switching terms of the AFSMC controller are continuous, therefore, the driving forces and the trajectories of the AFSMC controller are both smooth. The average SD of the SMC controller is 0.656 mm on two different trajectories and the AFSMC controller reduces it to 0.387 mm, which also indicates that the AFSMC controller can alleviate chattering behaviors. Moreover, the AFSMC controller can estimate friction forces as illustrated in Fig. 7(d1–d2)

Due to the above advantages, the AFSMC controller exhibits smaller errors compared with the SMC controller (Fig. 7(b1–b2)). The significant errors of the AFSMC controller happen exclusively at points where there is a discontinuity in desired velocities. The SMC controller generates an average RMSE of 1.336 mm (0.90% of the length of the continuum manipulator) and an SE of 3.001 mm. The AFSMC controller reduces the RMSE and SE to 0.618 mm (46.26% of the SMC controller) and 1.745 mm (58.15% of the SMC controller), respectively. A one-tailed Welch's t-test revealed a statistically significant reduction in tracking error for the AFSMC controller compared with the SMC controller ($t\,(8221.5) = -63.03$, $p < 0.001$). The effect size is quantified with Cohen's $d = -1.25$, demonstrating a large practical improvement. Such results indicate the effectiveness of the continuum manipulator modeling approach and the high trajectory tracking precision of the AFSMC controller on the physical manipulator.

3.2. Evaluations of adaptive fuzzy subcontrollers in the AFSMC controller

In this section, the individual effects of adaptive fuzzy subcontrollers $Fuzzy_f$ and $Fuzzy_s$ in the proposed AFSMC controller are further validated. Two groups of experiments were conducted with the same experimental configuration and controller parameter settings as Section 3.1. The first one is designed for the SMC

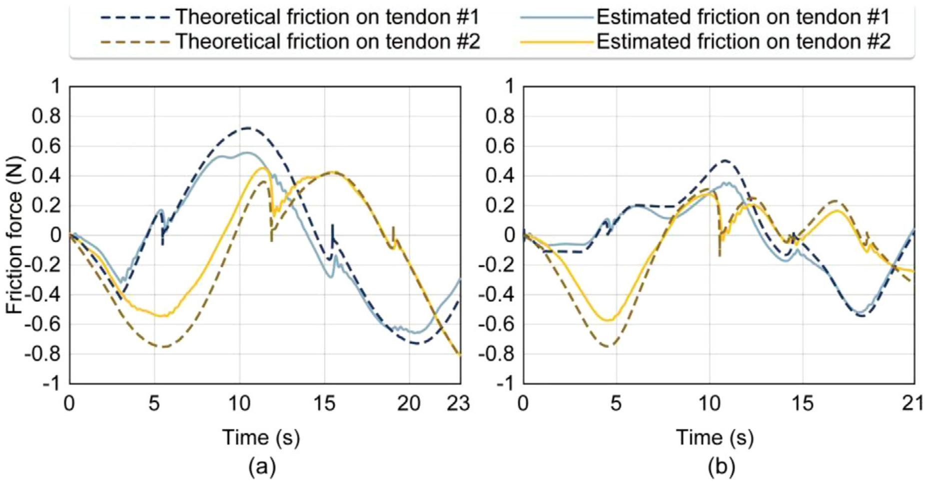

Fig. 6. Theoretical and estimated friction forces on both tendons during the trajectory tracking simulations. (a) On circular trajectory tracking. (b) On compound trajectory tracking.

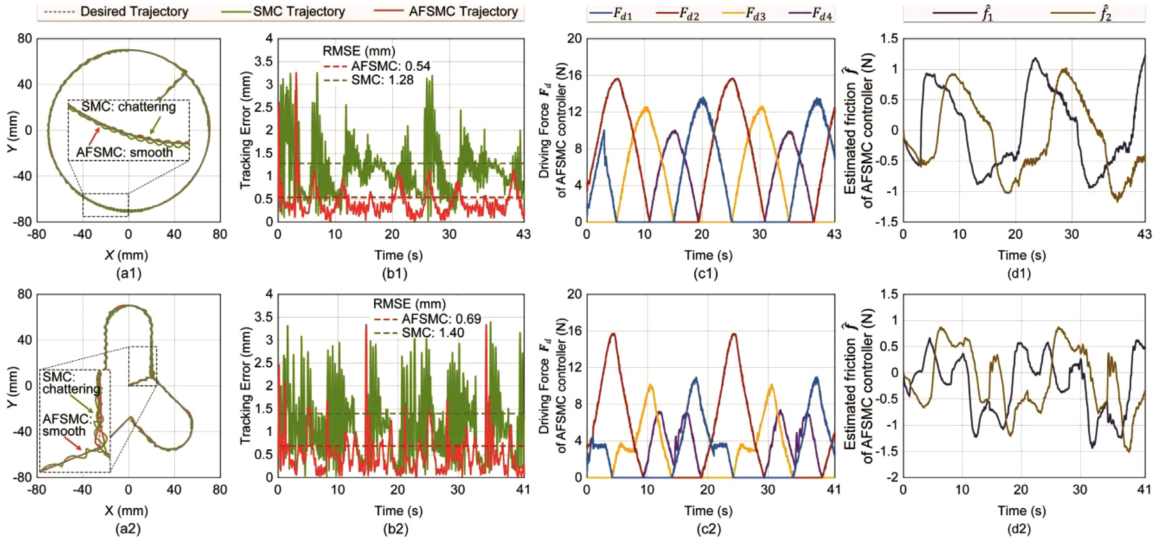

Fig. 7. The tracking performances, tracking error variations of the AFSMC and SMC controllers, and intermediate results of the AFSMC controller in free space experiments. (a1–a2) The measured circular and compound trajectories of both controllers with details. (b1–b2) The tracking error variations of both controllers on each trajectory. (c1–c2) The driving force variations calculated by the AFSMC controller on each trajectory. (d1–d2) The friction forces estimated by the AFSMC controller on each trajectory.

Table 1
Identified parameters of the continuum manipulator and controller parameter settings in experiments.

Manipulator parameter	Physical meaning	Value	Controller parameter	Value
L	Length of the central backbone	0.148 m	$\boldsymbol{\gamma}$	diag(20, 20)
H	Height of the end effector	0.044 m	$\boldsymbol{K}$	diag(4, 4)
R	Radius of the manipulator	0.01 m	$\boldsymbol{W}$	diag(1, 1)
m_1	1st centralized mass	0.019 kg	Γ_1	5×10^{-4}
m_2	2nd centralized mass	0.025 kg	Γ_2	5×10^{-4}
E	Young's modulus	56.278 Gpa	ϕ_1	2×10^{-3}
I	Cross-sectional inertia	$5.153 \times 10^{-13}\text{m}^4$	ϕ_2	2×10^{-3}

Table 2
Data analysis of the experimental results in free space.

Trajectory	Controller	RMSE (mm)	Relative RMSE	SD (mm)	Relative SD	SE (mm)
Circular	SMC	1.275	0.86%	0.575	0.39%	3.001
	AFSMC	0.543	0.37%	0.322	0.22%	1.745
Compound	SMC	1.396	0.94%	0.737	0.50%	–
	AFSMC	0.692	0.47%	0.451	0.30%	–
Mean value on two trajectories	SMC	1.336	0.90%	0.656	0.44%	3.001
	AFSMC	0.618	0.42%	0.387	0.26%	1.745

t-test results (on two trajectories): $t\,(8221.5) = -63.03$, $p < 0.001$, Cohen's $d = -1.25$ (large effect size).

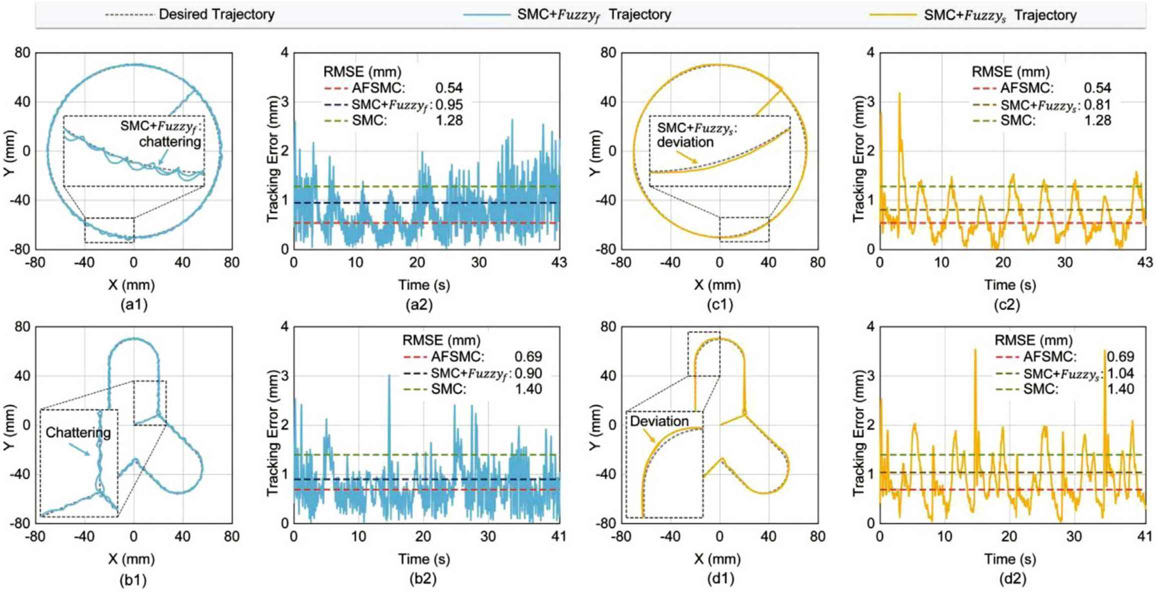

Fig. 8. The tracking performances and tracking error variations in evaluations of the adaptive fuzzy subcontrollers. (a1–b1) The measured circular and compound trajectories of the SMC controller with $Fuzzy_f$. (a2–b2) The tracking error variations of the SMC controller with $Fuzzy_f$ on each trajectory. (c1–d1) The measured circular and compound trajectories of the SMC controller with $Fuzzy_s$. (c2–d2) The tracking error variations of the SMC controller with $Fuzzy_s$on each trajectory.

Table 3
Data analysis in evaluations of the adaptive fuzzy subcontrollers.

Trajectory	Controller	RMSE (mm)	Relative RMSE	SD (mm)	Relative SD
Mean value on two trajectories	AFSMC	0.618	0.42%	0.387	0.26%
	SMC+$Fuzzy_f$	0.922	0.62%	0.463	0.31%
	SMC+$Fuzzy_s$	0.927	0.63%	0.489	0.33%
	SMC	1.336	0.90%	0.656	0.44%

controller with subcontrollers $Fuzzy_f$ (denoted as SMC_f), while the second one is for the SMC controller with $Fuzzy_s$ (denoted as SMC_s).

The experimental results of these single-module studies are presented in Fig. 8 and Table 3. The trajectories generated by SMC_f exhibit chattering behaviors with an average SD of 0.463 mm (120% of the AFSMC controller). This result verifies the effect of $Fuzzy_s$ to alleviate chattering. Meanwhile, the SMC_f reduces the average RMSE to 0.922 mm compared with 1.336 mm of the SMC controller. This result demonstrates that $Fuzzy_f$ can compensate for friction forces, thereby improving tracking accuracy. In addition, similar analyses can be conducted on the results of SMC_s to get the same conclusion. Overall, due to the respective effects of $Fuzzy_s$ and $Fuzzy_f$ to alleviate chattering and compensate for friction forces, the proposed AFSMC controller can achieve smooth and accurate trajectory tracking.

3.3. Trajectory tracking experiments for the AFSMC controller with distal loading

3.3.1. Trajectory tracking experiments under constant loading

The trajectory tracking experiments with constant external disturbance have been conducted to investigate the robustness of the proposed controller. Weights of 50 g/100 g were introduced to the manipulator at the beginning of the trajectory tracking as the disturbance (the setup of the weights is displayed in Fig. 9(a1–a3). The parameters of the continuum manipulator and controllers remain the same as enumerated in Table 1.

The trajectory tracking results with a 50 g loading are shown in Fig. 9, and the assessed errors with both 50 g and 100 g loadings are collected in Table 4. In the 50 g loading case, the SMC controller still exhibits chattering behaviors with an average SD of 1.725 mm, while the AFSMC controller reduces the SD to 0.817 mm with smoother trajectories. Notably, the SMC controller shows significant deviation, while the errors of the AFSMC controller are much smaller. The SMC controller generates an average RMSE of 6.348 mm (4.29% of the manipulator length) and an SE of 3.559 mm. The AFSMC controller reduces the RMSE to 2.176 mm (34.28% of the SMC controller) and the SE to 2.266 mm (63.67% of the SMC controller). In the 100 g loading case, although the tracking error of both controllers rises, the AFSMC controller still maintains a performance advantage with an RMSE of 3.87 mm, an SD of 1.534 mm, and an SE of 2.703 mm (26.02%, 44.18%, and 54.32% of the SMC controller, respectively). The main reason lies in the different designs of the switching terms. As indicated by Fig. 9(e1–e2), the magnitude of the fuzzy switching term $\hat{W}_2$ (exerted on tendon #2 in the vertical direction) of the AFSMC controller grows immediately after the loading time to counter the influence of disturbance. As a result, the driving force F_{d2} has a higher magnitude than that in free space tracking (Fig. 9(d1–d2)) and Fig. 7(c1–c2)). This is because the adaptive fuzzy subcontrollers $Fuzzy_s$ can dynamically adjust the magnitudes of the fuzzy switching terms according to the extent of external disturbances via adaptive laws. Nevertheless, the SMC controller maintains its switching term $W_2\text{sgn}(s_2)$ at a fixed magnitude (1N as shown in Table 1) without adjustment, thereby failing to effectively counteract disturbance effects.

3.3.2. Trajectory tracking experiments under variable loading

The tracking experiments under variable external disturbance were further performed by attaching a 50 g/100 g weight to the manipulator's distal tip through a sideways fixed pulley, as shown in Fig. 10(a1–a3). The direction of the external force applied to the manipulator changes continuously during the trajectory tracking, thereby serving as a variable disturbance.

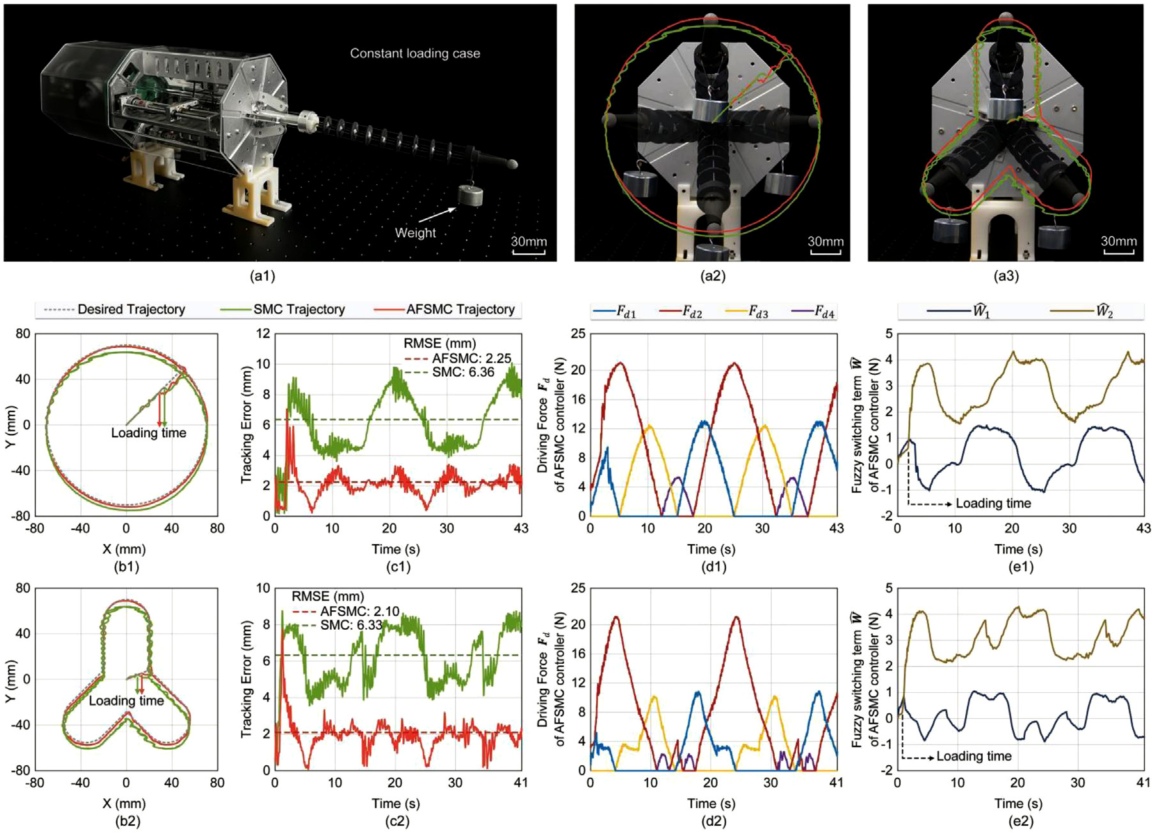

Fig. 9. The tracking performances and tracking error variations of the AFSMC and SMC controllers along with intermediate results of the AFSMC controller under the 50 g constant loading condition. (a1–a3) Side view and front view of the robotic system with constant loading. (b1–b2) The measured circular and compound trajectories of both controllers. (c1–c2) The tracking error variations of both controllers on each trajectory. (d1–d2) The driving force variations calculated by the AFSMC controller on each trajectory. (e1–e2) The fuzzy switching term variations calculated by the AFSMC controller on each trajectory.

Table 4
Data analysis of the experimental results under constant external disturbance.

Load (g)	Trajectory	Controller	RMSE (mm)	Relative RMSE	SD (mm)	Relative SD	SE (mm)
50	Circular	SMC	6.364	4.30%	1.944	1.31%	3.559
		AFSMC	2.253	1.52%	0.815	0.55%	2.266
	Compound	SMC	6.332	4.28%	1.505	1.02%	–
		AFSMC	2.099	1.42%	0.818	0.55%	–
	Mean value on two trajectories	SMC	6.348	4.29%	1.725	1.17%	3.559
		AFSMC	2.176	1.47%	0.817	0.55%	2.266
100	Circular	SMC	14.461	9.77%	3.565	2.41%	4.976
		AFSMC	3.994	2.70%	1.539	1.04%	2.703
	Compound	SMC	15.284	10.32%	3.378	2.28%	–
		AFSMC	3.746	2.53%	1.529	1.03%	–
	Mean value on two trajectories	SMC	14.873	10.04%	3.472	2.35%	4.976
		AFSMC	3.870	2.61%	1.534	1.04%	2.703

t-test results (on two trajectories, 50 g loading): $t\,(7173.0) = -150.54$, $p < 0.001$, Cohen's $d = -2.99$ (large effect size).
t-test results (on two trajectories, 100 g loading): $t\,(6923.7) = -202.18$, $p < 0.001$, Cohen's $d = -4.03$ (large effect size).

The tracking results under variable disturbance are summarized in Table 5 and results under the 50 g loading condition are illustrated in Fig. 10. The RMSEs of both controllers remain comparable to those observed under constant disturbance, though both controllers display slight increases in SEs and SDs due to the continuous fluctuation in external force direction. For instance, in the 50 g loading case, the SMC controller exhibits an average SD of 2.893 mm (1.95% of the manipulator's length) and an SE of 7.386 mm. The AFSMC controller reduces the SD and the SE to 1.032 mm and 4.342 mm (35.67% and 58.79% of the SMC controller respectively). Meanwhile, it is noteworthy that the magnitudes of both fuzzy switching terms $\hat{W}_1$ and $\hat{W}_2$ increase to counteract the variable-direction external force, which differs from the case with constant disturbance (Fig. 10(e1–e2)). Based on the experimental results in this section, it can be concluded that the AFSMC controller has high trajectory tracking robustness toward both constant and variable disturbance.

3.4. Experiments for the AFSMC controller on trajectories with different prescribed speeds

This section investigates the performances of the proposed AFSMC controller tracking trajectories with different speeds. The experiments are divided into three groups according to their prescribed speeds. In the first group Exp. D1, the tracking time is set as 20 s (21.99 mm/s for the circular path and 20.77 mm/s for the compound path). In the group Exp. D2 and Exp. D3, the tracking times are respectively set as 10 s and 6 s (the speeds are

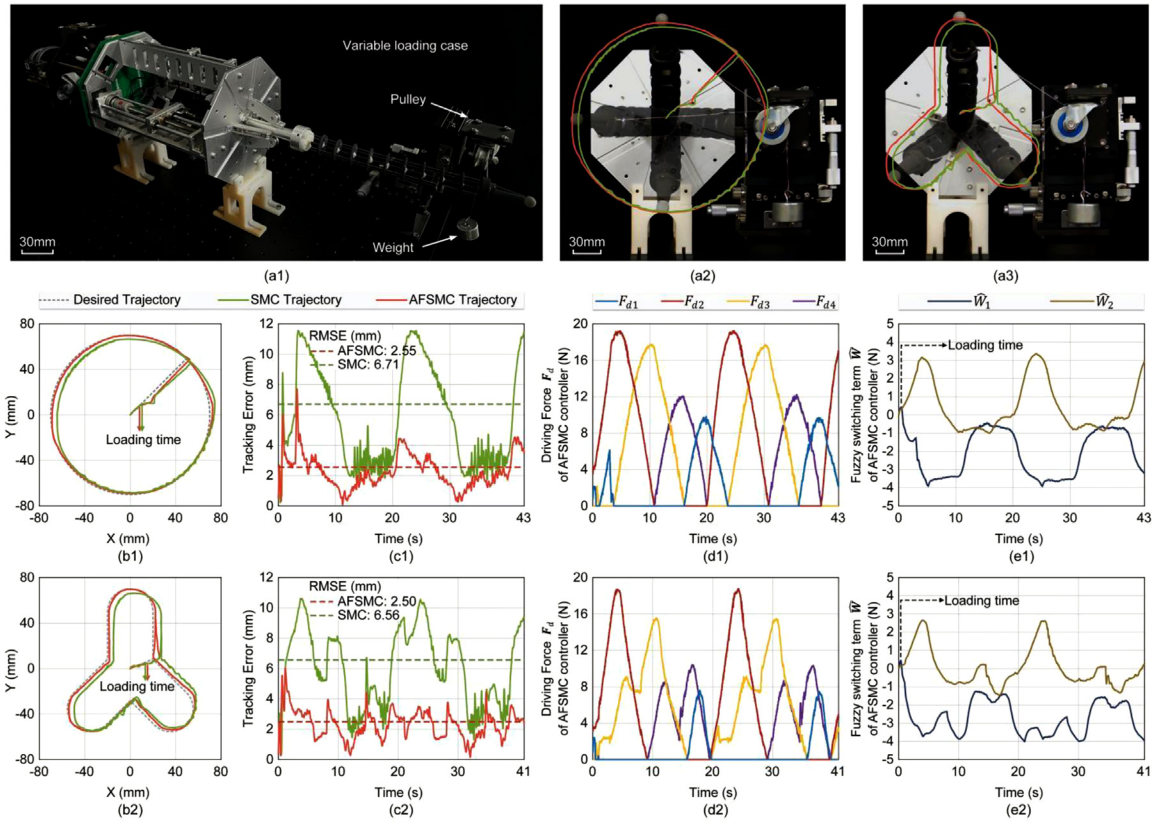

Fig. 10. The tracking performances and tracking error variations of AFSMC and SMC controllers along with intermediate results of the AFSMC controller under the 50 g variable loading condition. (a1–a3) Side view and front view of the robotic system with variable loading. (b1–b2) The measured circular and compound trajectories of both controllers. (c1–c2) The tracking error variations of both controllers on each trajectory. (d1–d2) The driving force variations calculated by the AFSMC controller on each trajectory. (e1–e2) The fuzzy switching term variations calculated by the AFSMC controller on each trajectory.

Table 5
Data analysis of the experimental results under variable external disturbance.

Load (g)	Trajectory	Controller	RMSE (mm)	Relative RMSE	SD (mm)	Relative SD	SE (mm)
50	Circular	SMC	6.712	4.54%	3.264	2.21%	7.386
		AFSMC	2.552	1.72%	1.127	0.76%	4.342
	Compound	SMC	6.562	4.43%	2.521	1.70%	–
		AFSMC	2.496	1.69%	0.936	0.63%	–
	Mean value on two trajectories	SMC	6.637	4.48%	2.893	1.95%	7.386
		AFSMC	2.524	1.71%	1.032	0.70%	4.342
100	Circular	SMC	13.104	8.85%	4.622	3.12%	7.531
		AFSMC	4.885	3.30%	1.656	1.12%	4.781
	Compound	SMC	14.581	9.85%	4.514	3.05%	–
		AFSMC	4.751	3.21%	1.553	1.05%	–
	Mean value on two trajectories	SMC	13.843	9.35%	4.568	3.09%	7.531
		AFSMC	4.818	3.26%	1.605	1.08%	4.781

t-test results (on two trajectories, 50 g loading): $t\,(6294.9) = -83.66$, $p < 0.001$, Cohen's $d = -1.67$ (large effect size).
t-test results (on two trajectories, 100 g loading): $t\,(6239.2) = -122.96$, $p < 0.001$, Cohen's $d = -2.45$ (large effect size).

separately doubled and tripled compared with Exp. D1). Moreover, the tracking time of the initial straight line from the center to the target trajectory remains the same (3 s for the circular path and 1 s for the compound path). A position controller based on pure kinematics was also implemented as the benchmark, which utilizes the standard resolved motion rate control (RMRC) method. As shown in [13], this RMRC controller can be formulated as:

$$\dot{\boldsymbol{q}}\,[k] = \boldsymbol{J}^{-1}\,[k]\left(\dot{\boldsymbol{p}}_d\,[k] + \boldsymbol{K}_p\left(\boldsymbol{p}_d\,[k] - \boldsymbol{p}\,[k]\right)\right) \tag{24}$$

where k denotes the time step, $\boldsymbol{K}_p$ represents its proportional parameters and $\boldsymbol{J}$ is the Jacobian defined in Eq. (3).

The trajectory tracking results under different speeds are illustrated in Fig. 11, and the corresponding errors are shown in Table 6. As the desired trajectory speeds increase, both the AFSMC and RMRC controllers exhibit increased errors (Fig. 11(a2–f2)). This trend is reasonable because, as the reference signal (desired trajectory) changes more rapidly, the control frequency stays constant due to the hardware constraint. Meanwhile, both controllers tend to generate larger errors at the points where there is a discontinuity in desired velocities. However, the AFSMC controller generally demonstrates smaller errors than the RMRC controller. The AFSMC controller generates an average RMSE of 0.618 mm in Exp. D1, 1.233 mm in Exp. D2, and 2.354 mm in Exp. D3 (1.0 mm, 1.8 mm, and 2.8 mm smaller than the RMRC controller, respectively). As computed, the disparities in RMSEs between the AFSMC and RMRC controllers exhibit an increasing trend at higher speeds. Firstly, this can be attributed to the meticulous design of the AFSMC controller, including fast response by the

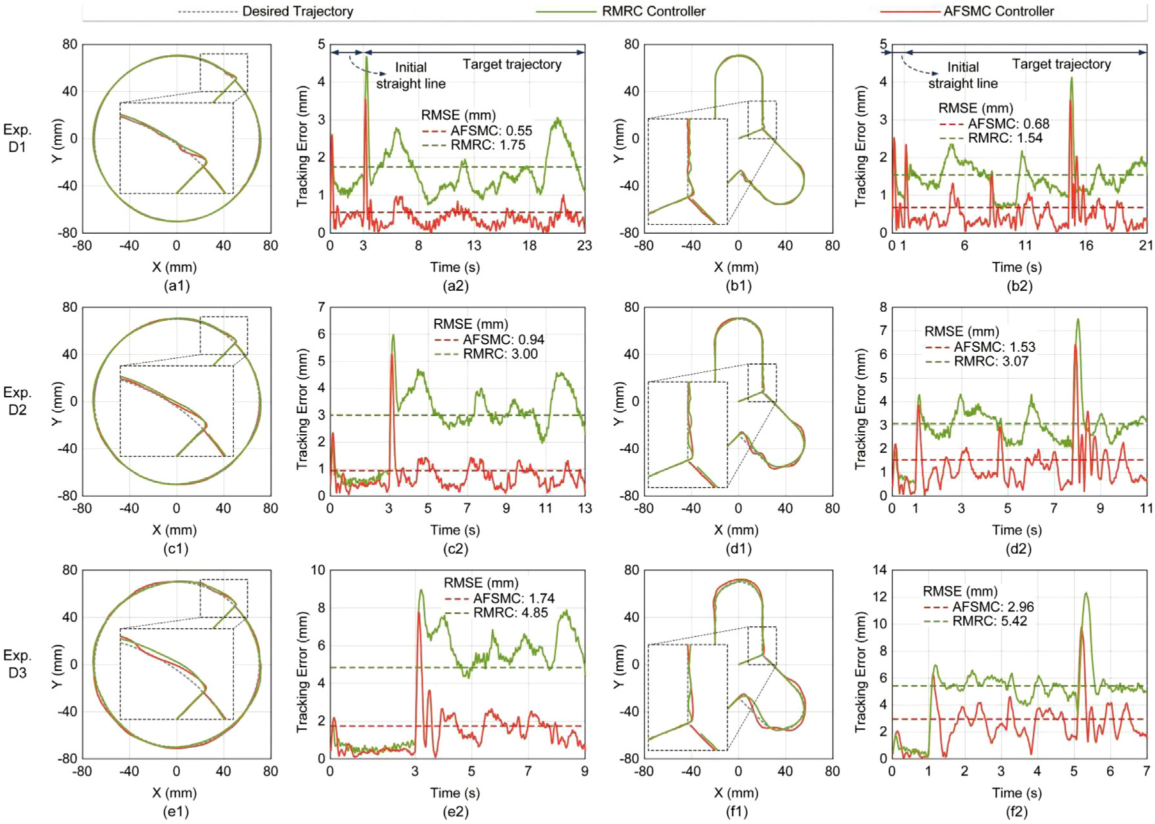

Fig. 11. The tracking performances and tracking error variations of the AFSMC and RMRC controllers under different prescribed speeds. (a1–b1) The measured circular and compound trajectories in Exp. D1. (a2–b2) The corresponding tracking error variations on each trajectory in Exp. D1. (c1–d1) The measured circular and compound trajectories in Exp. D2. (c2–d2) The corresponding tracking error variations on each trajectory in Exp. D2. (e1–f1) The measured circular and compound trajectories in Exp. D3. (e2–f2) The corresponding tracking error variations on each trajectory in Exp. D3.

Table 6
Tracking errors in the experiments with different speeds.

Trajectory	Experiment label	Controller	RMSE (mm)	Relative RMSE
Mean value on two trajectories	Exp. D1	RMRC	1.643	1.11%
		AFSMC	0.618	0.42%
	Exp. D2	RMRC	3.034	2.05%
		AFSMC	1.233	0.83%
	Exp. D3	RMRC	5.131	3.47%
		AFSMC	2.354	1.59%

Table 7
Dynamic terms on trajectories with different speeds.

Experiment label	Trajectory	Mean value of $\|M\ddot{q}_r + C\dot{q}_r\|$
Exp. D1	Circular	0.186 N
	Compound	0.181 N
Exp. D2	Circular	0.301 N
	Compound	0.340 N
Exp. D3	Circular	0.492 N
	Compound	0.671 N

SMC law and friction compensation by the adaptive fuzzy subcontrollers $Fuzzy_f$. Secondly, the AFSMC controller is designed based on the dynamic model, while the RMRC controller neglects the dynamic effects on these trajectories. As depicted in Table 7, the AFSMC controller generates dynamic terms to reduce the tracking error, and their magnitudes increase with higher speeds. These experimental results indicate that the AFSMC controller exhibits consistent and stable behaviors at different speeds. Furthermore, by incorporating dynamic effects, the AFSMC controller achieves higher tracking accuracy compared with the RMRC controller.

3.5. Discussion

The experimental results have validated that the proposed AFSMC controller for tendon-driven continuum manipulators can achieve smooth and accurate tracking of dynamic trajectories, with high robustness toward external disturbances. These performances are ensured by the appropriate integration of an SMC control law and adaptive fuzzy subcontrollers. In addition, the contributions of the subcontrollers $Fuzzy_f$ to compensate for friction forces and subcontrollers $Fuzzy_s$ to alleviate chattering have been separately validated. Moreover, the behavior of the AFSMC controller at different tracking speeds is consistent and stable, with higher accuracy than the RMRC controller which purely relies on kinematics.

In experimental validations, controllers tend to exhibit larger errors at points with discontinuity of desired velocities. This is primarily because the controllers may not respond quickly enough to compensate for the sudden changes. From a control perspective, these points can better investigate the controllers' stability and tracking performances. However, in practical applications, avoiding the presence of these points in desired trajectories is essential to ensure both safe and accurate manipulation. Thus, motion planning methods for avoiding jerk movement are important and will be explored in future research.

For trajectory tracking experiments in free space, only the estimated friction forces are recorded, because it is challenging to measure the actual friction forces along tendons. Therefore, the simulation studies in Appendix B serve as supplementary proof of the AFSMC controller's friction estimation ability. In the experiments with both constant and variable loading, the AFSMC controller demonstrates superior robustness than the SMC controller. However, it was observed that the deviation of the AFSMC controller slightly got larger as the loading increased. To further enhance robustness, Eq. (10) could be extended to incorporate fuzzy PID [21] or neural network PID methodologies.

In the experiments with different prescribed speeds, the AFSMC controller exhibits increased errors at higher speeds. To lessen the tracking error, a viable solution is to update the hardware for a higher control frequency. Furthermore, it is noteworthy that the trajectories generated by the RMRC controller lag behind the desired trajectories, evident at the end of the tracking process. Therefore, although the RMRC controller occasionally follows the geometric path more closely, its performance in accurately tracking the time-parameterized desired trajectory is inferior. Consequently, the AFSMC controller with enhanced tracking accuracy at various speeds is more suitable for surgical applications, where precise tracking of trajectories with different speeds is imperative (Fig. 1). Moreover, the proposed AFSMC controller will be implemented on continuum manipulators [42,43] specifically designed for targeted medical applications in future research. Additionally, the tip position feedback by the binocular visual measurement unit will be replaced by vision-based methods [44,45] through the binocular endoscope to achieve practical visual servo control [46] under medical situations.

4. Conclusion

In this work, an AFSMC controller for the tendon-driven continuum manipulator is proposed, which merges SMC with two independent groups of adaptive fuzzy subcontrollers $Fuzzy_f$ and $Fuzzy_s$. The subcontrollers $Fuzzy_f$ can estimate and compensate for friction forces along tendons. The $Fuzzy_s$ adapts the traditional switching terms of SMC to reduce chattering and enhance robustness. To prevent tendon slack, an antagonistic control strategy is designed based on the antagonistic arrangement of tendons. Experimental results demonstrate that the AFSMC controller not only addresses the tendon friction and slack issues but also exhibits high control accuracy and robustness during trajectory tracking. Meanwhile, simulation results validate the effectiveness of the friction estimation capability by incorporating a theoretical friction model. In addition, the contributions of adaptive fuzzy subcontrollers $Fuzzy_f$ and $Fuzzy_s$ are separately evaluated. Furthermore, the AFSMC controller exhibits consistent behaviors at different speeds and higher accuracy than the RMRC controller. These benefits can enable manipulators to maintain accurate tracking not only in the manipulation stage of surgeries to achieve safe tissue interaction but also in the approach stage to realize efficient surgical navigation and inspection. In future research, the proposed controller will be extended to address the segment coupling issue in multiple-segment manipulators [47]. Moreover, the chained beam model, which maintains its accuracy even under significant deflections, will be integrated into the controller design framework to further enhance modeling precision [48,49]. Furthermore, fiber Bragg grating (FBG) sensing techniques [5,50,51] can be integrated to provide force and shape feedback, enabling interaction control along the entire length of the manipulator.

CRediT authorship contribution statement

Pengyu Du: Writing – original draft, Validation, Methodology. **Jianxiong Hao:** Writing – original draft, Methodology, Data curation. **Kun Qian:** Writing – original draft, Supervision, Methodology. **Yue Zhang:** Writing – review & editing, Visualization, Validation, Data curation. **Zhiqiang Zhang:** Writing – review & editing, Supervision, Project administration, Methodology, Investigation, Funding acquisition. **Chaoyang Shi:** Writing – review & editing, Methodology, Investigation, Funding acquisition, Conceptualization.

Declaration of competing interest

The authors declare that they have no known competing financial interests or personal relationships that could have appeared to influence the work reported in this paper.

Acknowledgments

This work is partly supported by the National Natural Science Foundation of China (92148201, 52475029). This work is also supported by International Institute for Innovative Design and Intelligent Manufacturing of Tianjin University in Zhejiang, Shaoxing 312000, China.

Declaration of competing interest

The authors declare that they have no known competing financial interests or personal relationships that could have appeared to influence the work reported in this paper.

Appendix A. Stability analysis of the AFSMC controller

The dynamic model of the continuum manipulator is rewritten as Eq. (A.1), and an additional term $\boldsymbol{d}$ which denotes external disturbance is added for stability proof.

$$\boldsymbol{M}\left(\boldsymbol{q}\right)\ddot{\boldsymbol{q}}+\boldsymbol{C}\left(\boldsymbol{q},\dot{\boldsymbol{q}}\right)\dot{\boldsymbol{q}}+\boldsymbol{N}\left(\boldsymbol{q}\right)+\boldsymbol{f}+\boldsymbol{d}=\boldsymbol{F}_d. \tag{A.1}$$

Lemma 1. *The matrix* $\boldsymbol{C}\left(\boldsymbol{q},\dot{\boldsymbol{q}}\right)$ *is obtained utilizing Christoffel symbols, thus* $\dot{\boldsymbol{M}}\left(\boldsymbol{q}\right)-2\boldsymbol{C}\left(\boldsymbol{q},\dot{\boldsymbol{q}}\right)$ *is skew-symmetric [39].*

The optimal parameter $\boldsymbol{\theta}_f^*$ of adaptive fuzzy subcontrollers $Fuzzy_f$ can be defined as that which achieves the minimal approximation error.

$$\boldsymbol{\theta}_f^*=\arg\min_{\boldsymbol{\theta}_f\in\Theta_f}\left(\sup\left\|\hat{\boldsymbol{f}}\left(\boldsymbol{q},\dot{\boldsymbol{q}}|\boldsymbol{\theta}_f\right)-\boldsymbol{f}\right\|_\infty\right). \tag{A.2}$$

The switching gains $\boldsymbol{W}^*$ of the desired switching term $\boldsymbol{W}^*\mathrm{sgn}\left(\boldsymbol{s}\right)$ should be the upper bound of disturbances $\boldsymbol{d}$, as represented in the following condition.

$$W_k^*\geq d_k, k\in\left\{1,2\right\}. \tag{A.3}$$

Then the optimal parameter $\boldsymbol{\theta}_W^*$ can be defined similarly as:

$$\boldsymbol{\theta}_W^* = \arg\min_{\boldsymbol{\theta}_W \in \Theta_W} \left(\sup \left\| \hat{\boldsymbol{W}} \left(\boldsymbol{s} | \boldsymbol{\theta}_W \right) - \boldsymbol{W}^* \mathrm{sgn} \left(\boldsymbol{s} \right) \right\|_\infty \right). \tag{A.4}$$

Errors in the parameters $\boldsymbol{\theta}_{f_k}$ and $\boldsymbol{\theta}_{W_k}$ can be defined as follows ($\boldsymbol{\theta}_f = [\boldsymbol{\theta}_{f_1} \boldsymbol{\theta}_{f_2}]$ and $\boldsymbol{\theta}_W = [\boldsymbol{\theta}_{W_1} \boldsymbol{\theta}_{W_2}]$).

$$\tilde{\boldsymbol{\theta}}_{f_k} = \boldsymbol{\theta}_{f_k}^* - \boldsymbol{\theta}_{f_k}, k \in \{1, 2\} \tag{A.5}$$

$$\tilde{\boldsymbol{\theta}}_{W_k} = \boldsymbol{\theta}_{W_k}^* - \boldsymbol{\theta}_{W_k}, k \in \{1, 2\}. \tag{A.6}$$

With the above optimal parameters $\boldsymbol{\theta}_f^*$ and $\boldsymbol{\theta}_W^*$, the minimal approximation errors of the adaptive fuzzy subcontrollers can be represented as:

$$\delta_f = \boldsymbol{f} - \hat{\boldsymbol{f}} \left(\boldsymbol{q}, \dot{\boldsymbol{q}} | \boldsymbol{\theta}_f^* \right) \tag{A.7}$$

$$\delta_W = \boldsymbol{W}^* \mathrm{sgn} \left(\boldsymbol{s} \right) - \hat{\boldsymbol{W}} \left(\boldsymbol{s} | \boldsymbol{\theta}_W^* \right). \tag{A.8}$$

Because adaptive fuzzy control can approximate a function with any given accuracy, the minimal approximation errors $\boldsymbol{\delta}_f$ and $\boldsymbol{\delta}_W$ are small and bounded, which leads to the following condition.

$$\begin{cases} \left| \delta_{f_k} \right| \le \alpha_k \left| s_k \right| \\ \left| \delta_{W_k} \right| \le \beta_k \left| s_k \right|, \end{cases} \quad \alpha_k > 0, \beta_k > 0, k \in \{1, 2\}. \tag{A.9}$$

The stability of the AFSMC controller and the adaptive laws (16) and (19) can be derived by considering the following Lyapunov function candidate, where $\Gamma_k > 0$ and $\phi_k > 0$.

$$V = \tfrac{1}{2} \boldsymbol{s}^{\mathrm{T}} \boldsymbol{M} \boldsymbol{s} + \tfrac{1}{2} \textstyle\sum_{k=1}^{2} \Gamma_k \tilde{\boldsymbol{\theta}}_{f_k}^{\mathrm{T}} \tilde{\boldsymbol{\theta}}_{f_k} + \tfrac{1}{2} \textstyle\sum_{k=1}^{2} \phi_k \tilde{\boldsymbol{\theta}}_{W_k}^{\mathrm{T}} \tilde{\boldsymbol{\theta}}_{W_k}. \tag{A.10}$$

The derivative of the above function w.r.t. time is obtained by combining Eqs. (21), (A.1) and (A.10).

$$\begin{aligned} \dot{V} &= \boldsymbol{s}^{\mathrm{T}} \boldsymbol{M} \dot{\boldsymbol{s}} + \frac{1}{2} \boldsymbol{s}^{\mathrm{T}} \dot{\boldsymbol{M}} \boldsymbol{s} + \sum_{k=1}^{2} \left(\Gamma_k \tilde{\boldsymbol{\theta}}_{f_k}^{\mathrm{T}} \dot{\tilde{\boldsymbol{\theta}}}_{f_k} + \phi_k \tilde{\boldsymbol{\theta}}_{W_k}^{\mathrm{T}} \dot{\tilde{\boldsymbol{\theta}}}_{W_k} \right) \\ & \textit{using} \quad \textit{Lemma} 1: \\ &= \boldsymbol{s}^{\mathrm{T}} \boldsymbol{M} \left(\ddot{\boldsymbol{q}} - \ddot{\boldsymbol{q}}_{\boldsymbol{r}} \right) + \boldsymbol{s}^{\mathrm{T}} \boldsymbol{C} \boldsymbol{s} + \sum_{k=1}^{2} \left(\Gamma_k \tilde{\boldsymbol{\theta}}_{f_k}^{\mathrm{T}} \dot{\tilde{\boldsymbol{\theta}}}_{f_k} + \phi_k \tilde{\boldsymbol{\theta}}_{W_k}^{\mathrm{T}} \dot{\tilde{\boldsymbol{\theta}}}_{W_k} \right) \\ &= \boldsymbol{s}^{\mathrm{T}} \left(\hat{\boldsymbol{f}} - \boldsymbol{f} - \hat{\boldsymbol{W}} - \boldsymbol{K} \boldsymbol{s} - \boldsymbol{d} \right) + \sum_{k=1}^{2} \left(\Gamma_k \tilde{\boldsymbol{\theta}}_{f_k}^{\mathrm{T}} \dot{\tilde{\boldsymbol{\theta}}}_{f_k} + \phi_k \tilde{\boldsymbol{\theta}}_{W_k}^{\mathrm{T}} \dot{\tilde{\boldsymbol{\theta}}}_{W_k} \right) \\ &= -\boldsymbol{s}^{\mathrm{T}} \delta_f + \boldsymbol{s}^{\mathrm{T}} \delta_W - \boldsymbol{s}^{\mathrm{T}} \boldsymbol{d} - \boldsymbol{s}^{\mathrm{T}} \boldsymbol{W}^* \mathrm{sgn} \left(\boldsymbol{s} \right) - \boldsymbol{s}^{\mathrm{T}} \boldsymbol{K} \boldsymbol{s} \\ & \quad - \sum_{k=1}^{2} \left(\Gamma_k \tilde{\boldsymbol{\theta}}_{f_k}^{\mathrm{T}} \dot{\boldsymbol{\theta}}_{f_k} + s_k \tilde{\boldsymbol{\theta}}_{f_k}^{\mathrm{T}} \boldsymbol{\xi} \left(\boldsymbol{q}, \dot{\boldsymbol{q}} \right) \right) \\ & \quad - \sum_{k=1}^{2} \left(\phi_k \tilde{\boldsymbol{\theta}}_{W_k}^{\mathrm{T}} \dot{\boldsymbol{\theta}}_{W_k} - s_k \tilde{\boldsymbol{\theta}}_{W_k}^{\mathrm{T}} \boldsymbol{\xi} \left(s_k \right) \right). \end{aligned}$$

Substituting Eqs. (16) and (19) into the above equation leads to:

$$\dot{V} = -\boldsymbol{s}^{\mathrm{T}} \delta_f + \boldsymbol{s}^{\mathrm{T}} \delta_W - \boldsymbol{s}^{\mathrm{T}} \boldsymbol{d} - \boldsymbol{s}^{\mathrm{T}} \boldsymbol{W}^* \mathrm{sgn} \left(\boldsymbol{s} \right) - \boldsymbol{s}^{\mathrm{T}} \boldsymbol{K} \boldsymbol{s}. \tag{A.11}$$

Considering Eq. (A.3), it can be derived that:

$$\dot{V} \le -\boldsymbol{s}^{\mathrm{T}} \delta_f + \boldsymbol{s}^{\mathrm{T}} \delta_W - \boldsymbol{s}^{\mathrm{T}} \boldsymbol{K} \boldsymbol{s}. \tag{A.12}$$

Based on Eq. (A.9), it can be further written as follows, where $\boldsymbol{\alpha} = \mathrm{diag}(\alpha_1, \alpha_2)$, $\boldsymbol{\beta} = \mathrm{diag}(\beta_1, \beta_2)$.

$$\dot{V} \le \boldsymbol{s}^{\mathrm{T}} \left(\boldsymbol{\alpha} + \boldsymbol{\beta} \right) \boldsymbol{s} - \boldsymbol{s}^{\mathrm{T}} \boldsymbol{K} \boldsymbol{s}. \tag{A.13}$$

Because the approximation errors $\boldsymbol{\delta}_f$ and $\boldsymbol{\delta}_W$ are small, the α_k and β_k in Eq. (A.9) are small numbers, and the following assumption makes sense.

Assumption 1. The elements of the diagonal positive definite matrix $\boldsymbol{K}$ are big enough to counter the influence of $\boldsymbol{\delta}_f$ and $\boldsymbol{\delta}_W$, i.e., $K_i > \alpha_i + \beta_i$, $i \in \{1, 2\}$.

Based on Assumption 1, it can be further concluded from Eq. (A.13) that:

$$\dot{V} \le -\boldsymbol{s}^{\mathrm{T}} \boldsymbol{K}' \boldsymbol{s} \tag{A.14}$$

where $\boldsymbol{K}' = \boldsymbol{K} - (\boldsymbol{\alpha} + \boldsymbol{\beta})$ is a positive definite matrix. Thus, the derivative of the Lyapunov function (A.10) is ensured to be negative definite, which implies the asymptotic stability of the proposed controller.

Appendix B. Trajectory tracking simulations for the AFSMC controller

This section implements simulations of the continuum manipulator in MATLAB® 2019a (MathWorks, USA) to test the AFSMC controller's trajectory tracking performances and friction estimation capability. The target trajectories are kept the same as those in experiments and the SMC controller serves as the benchmark.

To verify the AFSMC controller's ability to estimate the friction, a theoretical friction model was incorporated, which utilizes the Dahl friction formulation:

$$\tfrac{df_D}{dl} = \sigma \left(1 - \tfrac{f_D}{f_c} \mathrm{sgn} \left(\dot{l} \right) \right)^{\alpha} \tag{B.1}$$

where f_D denotes the Dahl friction force, and f_c represents the Coulomb friction force. The reference [28] proves that the Dahl model has sufficient accuracy for the tendon-driven continuum robot scenario. However, the Coulomb friction force in the above model varies with the tendon tension and the bending angle of the robot. In this simulation, it is assumed that the Coulomb friction force is derived utilizing the capstan equation:

$$f_c = F_d \left(1 - e^{-\mu\theta} \right) \tag{B.2}$$

where F_d denotes the driving force calculated by the controller, and μ is the friction coefficient.

The parameters of the simulated continuum manipulator and controllers are listed in Table B.1, and simulation results are presented in Fig. B.1. The driving forces calculated by the SMC controller exhibit high-frequency variations while the curves of driving forces calculated by the AFSMC controller are smoother. As a result, the trajectories generated by the two controllers show chattering behaviors and smooth paths respectively. It indicates the effectiveness of $Fuzzy_s$ that provides continuous fuzzy switching terms. The capability of the proposed AFSMC controller to estimate the friction forces along the driving tendons during the trajectory tracking process was also evaluated, which has been illustrated in Fig. 6.

Overall, due to the chattering behaviors and lack of compensation for friction forces, the SMC controller generates larger tracking errors than the AFSMC controller (Fig. B.1 (b1–b2)). The SMC controller has an average RMSE of 1.288 mm (0.64% of the length of the continuum manipulator) on two different trajectories. However, the AFSMC controller reduces the RMSE to 0.305 mm (23.7% of the SMC controller). These simulation results demonstrate that the AFSMC controller can estimate and compensate for internal friction forces and achieve smooth and accurate trajectory tracking.

Appendix C. Supplementary data

Supplementary material related to this article can be found online at https://doi.org/10.1016/j.birob.2025.100234.

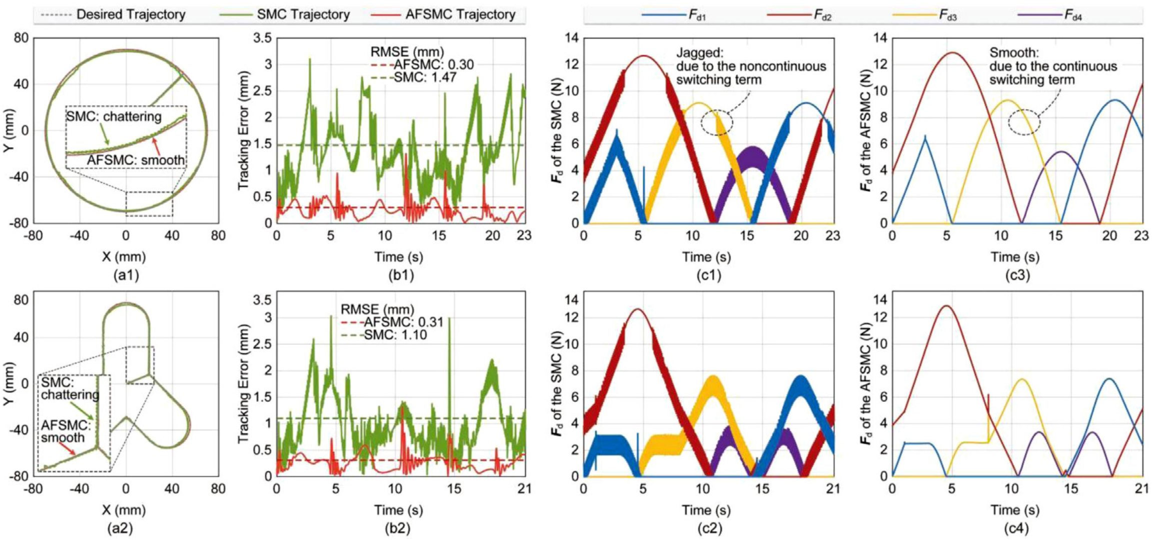

Fig. B.1. The tracking performances, tracking error variations, and driving force variations of the SMC and AFSMC controllers in simulations. (a1–a2) The measured circular and compound trajectories of both controllers with details. (b1–b2) The tracking error variations of both controllers on each trajectory. (c1–c2) The driving force variations calculated by the SMC controller on each trajectory. (c3–c4) The driving force variations calculated by the AFSMC controller on each trajectory.

Table B.1
Continuum manipulator and controller parameter settings in simulations.

Manipulator parameter	Physical meaning	Value	Controller parameter	Value
L	Length of the central backbone	0.2m	$\boldsymbol{\gamma}$	diag(15, 15)
H	Height of the end effector	0.03m	$\boldsymbol{K}$	diag(1.2, 1, 2)
R	Radius of the manipulator	0.01m	$\boldsymbol{W}$	diag(0.5, 0.5)
m_1	1st centralized mass	0.02kg	Γ_1	5×10^{-4}
m_2	2nd centralized mass	0.03kg	Γ_2	5×10^{-4}
E	Young's modulus	60Gpa	ϕ_1	5×10^{-3}
I	Cross-sectional inertia	$5.153 \times 10^{-13}\text{m}^4$	ϕ_2	5×10^{-3}

References

[1] P.E. Dupont, B.J. Nelson, M. Goldfarb, B. Hannaford, A. Menciassi, M.K. O'Malley, N. Simaan, P. Valdastri, G.-Z. Yang, A decade retrospective of medical robotics research from 2010 to 2020, Sci. Robot. 6 (2021) eabi8017, http://dx.doi.org/10.1126/scirobotics.abi8017.

[2] B. Lin, S. Song, J. Wang, Variable stiffness methods of flexible robots for minimally invasive surgery: A review, Biomim. Intell. Robot. 4 (2024) 100168, http://dx.doi.org/10.1016/j.birob.2024.100168.

[3] Z. Lin, Z. Xu, H. Liu, X. Wang, X. Ai, C. Zhou, B. Huang, W. Chen, G.-Z. Yang, A. Gao, Robotic manipulator-assisted omnidirectional augmented reality for endoluminal intervention telepresence, Adv. Intell. Syst. 6 (2024) 2300373, http://dx.doi.org/10.1002/aisy.202300373.

[4] P.E. Dupont, N. Simaan, H. Choset, C. Rucker, Continuum robots for medical interventions, Proc. IEEE 110 (2022) 847–870, http://dx.doi.org/10.1109/JPROC.2022.3141338.

[5] Chaoyang Shi, Xiongbiao Luo, Peng Qi, Tianliang Li, Shuang Song, Z. Najdovski, T. Fukuda, H. Ren, Shape sensing techniques for continuum robots in minimally invasive surgery: A survey, IEEE Trans. Biomed. Eng. 64 (2017) 1665–1678, http://dx.doi.org/10.1109/TBME.2016.2622361.

[6] D.A. Troncoso, J.A. Robles-Linares, M. Russo, M.A. Elbanna, S. Wild, X. Dong, A. Mohammad, J. Kell, A.D. Norton, D. Axinte, A continuum robot for remote applications: From industrial to medical surgery with slender continuum robots, IEEE Robot. Autom. Mag. 30 (2023) 94–105, http://dx.doi.org/10.1109/MRA.2022.3223220.

[7] Y. Lei, F. Du, H. Song, L. Zhang, Design and kinematics analysis of a cable-stayed notch manipulator for transluminal endoscopic surgery, Biomim. Intell. Robot. 4 (2024) 100191, http://dx.doi.org/10.1016/j.birob.2024.100191.

[8] D. Song, S. Wang, Z. Zhang, X. Yu, C. Shi, A novel continuum overtube with improved triangulation for flexible robotic endoscopy, IEEE Trans. Med. Robot. Bionics 5 (2023) 657–668, http://dx.doi.org/10.1109/TMRB.2023.3294527.

[9] M. Russo, S.M.H. Sadati, X. Dong, A. Mohammad, I.D. Walker, C. Bergeles, K. Xu, D.A. Axinte, Continuum robots: An overview, Adv. Intell. Syst. 5 (2023) 2200367, http://dx.doi.org/10.1002/aisy.202200367.

[10] R.J. Webster, B.A. Jones, Design and kinematic modeling of constant curvature continuum robots: A review, Int. J. Robot. Res. 29 (2010) 1661–1683, http://dx.doi.org/10.1177/0278364910368147.

[11] X. Zhang, Y. Liu, D.T. Branson, C. Yang, J.S. Dai, R. Kang, Variable-gain control for continuum robots based on velocity sensitivity, Mech. Mach. Theory 168 (2022) 104618, http://dx.doi.org/10.1016/j.mechmachtheory.2021.104618.

[12] J. Hao, K. Zhang, Z. Zhang, S. Wang, C. Shi, An online model-free adaptive tracking controller for cable-driven medical continuum manipulators, IEEE Trans. Med. Robot. Bionics 5 (2023) 623–635, http://dx.doi.org/10.1109/TMRB.2023.3291024.

[13] T. Mahl, A. Hildebrandt, O. Sawodny, A variable curvature continuum kinematics for kinematic control of the bionic handling assistant, IEEE Trans. Robot. 30 (2014) 935–949, http://dx.doi.org/10.1109/TRO.2014.2314777.

[14] S. Neppalli, M.A. Csencsits, B.A. Jones, I. Walker, A geometrical approach to inverse kinematics for continuum manipulators, in: 2008 IEEE/RSJ International Conference on Intelligent Robots and Systems, IEEE, Nice, 2008, pp. 3565–3570, http://dx.doi.org/10.1109/IROS.2008.4651125.

[15] K. Qiu, J. Zhang, D. Sun, R. Xiong, H. Lu, Y. Wang, An efficient multi-solution solver for the inverse kinematics of 3-section constant-curvature robots, in: Robotics: Science and Systems XIX, Robotics: Science and Systems Foundation, 2023, http://dx.doi.org/10.15607/RSS.2023.XIX.091.

[16] H. Li, L. Xun, G. Zheng, F. Renda, Discrete cosserat static model-based control of soft manipulator, IEEE Robot. Autom. Lett. 8 (2023) 1739–1746, http://dx.doi.org/10.1109/LRA.2023.3243799.

[17] X. Huang, J. Zou, G. Gu, Kinematic modeling and control of variable curvature soft continuum robots, IEEE/ASME Trans. Mechatron. 26 (2021) 3175–3185, http://dx.doi.org/10.1109/TMECH.2021.3055339.

[18] V. Falkenhahn, A. Hildebrandt, R. Neumann, O. Sawodny, Dynamic control of the bionic handling assistant, IEEE/ASME Trans. Mechatron. 22 (2017) 6–17, http://dx.doi.org/10.1109/TMECH.2016.2605820.

[19] R.K. Katzschmann, C.D. Santina, Y. Toshimitsu, A. Bicchi, D. Rus, Dynamic motion control of multi-segment soft robots using piecewise constant curvature matched with an augmented rigid body model, in: 2019 2nd IEEE International Conference on Soft Robotics, RoboSoft, IEEE, Seoul, Korea (South), 2019, pp. 454–461, http://dx.doi.org/10.1109/ROBOSOFT.2019.8722799.

[20] C. Della Santina, R.K. Katzschmann, A. Bicchi, D. Rus, Model-based dynamic feedback control of a planar soft robot: trajectory tracking and interaction with the environment, Int. J. Robot. Res. 39 (2020) 490–513, http://dx.doi.org/10.1177/0278364919897292.

[21] Y. Ma, Q. Wu, Z. Qiu, Y. Fang, N. Sun, Modeling and precise tracking control of spatial bending pneumatic soft actuators, Biomim. Intell. Robot. 4 (2024) 100192, http://dx.doi.org/10.1016/j.birob.2024.100192.

[22] A.D. Kapadia, K.E. Fry, I.D. Walker, Empirical investigation of closed-loop control of extensible continuum manipulators, in: 2014 IEEE/RSJ International Conference on Intelligent Robots and Systems, IEEE, Chicago, IL, USA, 2014, pp. 329–335, http://dx.doi.org/10.1109/IROS.2014.6942580.

[23] A. Kazemipour, O. Fischer, Y. Toshimitsu, K.W. Wong, R.K. Katzschmann, Adaptive dynamic sliding mode control of soft continuum manipulators, in: 2022 International Conference on Robotics and Automation, ICRA, IEEE, Philadelphia, PA, USA, 2022, pp. 3259–3265, http://dx.doi.org/10.1109/ICRA46639.2022.9811715.

[24] X. Shao, P. Pustina, M. Stölzle, G. Sun, A. De Luca, L. Wu, C.D. Santina, Model-based control for soft robots with system uncertainties and input saturation, IEEE Trans. Ind. Electron. (2023) 1–10, http://dx.doi.org/10.1109/TIE.2023.3303636.

[25] R. Kang, Y. Guo, L. Chen, D.T. Branson, J.S. Dai, Design of a pneumatic muscle based continuum robot with embedded tendons, IEEE/ASME Trans. Mechatron. 22 (2017) 751–761, http://dx.doi.org/10.1109/TMECH.2016.2636199.

[26] J. Hao, Z. Zhang, S. Wang, C. Shi, 2D shape estimation of a pneumatic-driven soft finger with a large bending angle based on learning from two sensing modalities, Adv. Intell. Syst. 5 (2023) 2200324, http://dx.doi.org/10.1002/aisy.202200324.

[27] H. Yuan, L. Zhou, W. Xu, A comprehensive static model of cable-driven multi-section continuum robots considering friction effect, Mech. Mach. Theory 135 (2019) 130–149, http://dx.doi.org/10.1016/j.mechmachtheory.2019.02.005.

[28] J. Jung, R.S. Penning, M.R. Zinn, A modeling approach for robotic catheters: effects of nonlinear internal device friction, Adv. Robot. 28 (2014) 557–572, http://dx.doi.org/10.1080/01691864.2013.879371.

[29] G. Subramani, M.R. Zinn, Tackling friction - an analytical modeling approach to understanding friction in single tendon driven continuum manipulators, in: 2015 IEEE International Conference on Robotics and Automation, ICRA, IEEE, Seattle, WA, USA, 2015, pp. 610–617, http://dx.doi.org/10.1109/ICRA.2015.7139242.

[30] R. Roy, L. Wang, N. Simaan, Modeling and estimation of friction, extension, and coupling effects in multisegment continuum robots, IEEE/ASME Trans. Mechatron. 22 (2017) 909–920, http://dx.doi.org/10.1109/TMECH.2016.2643640.

[31] Y. Liu, F. Alambeigi, Effect of external and internal loads on tension loss of tendon-driven continuum manipulators, IEEE Robot. Autom. Lett. 6 (2021) 1606–1613, http://dx.doi.org/10.1109/LRA.2021.3058913.

[32] R.E. Goldman, A. Bajo, N. Simaan, Compliant motion control for multisegment continuum robots with actuation force sensing, IEEE Trans. Robot. 30 (2014) 890–902, http://dx.doi.org/10.1109/TRO.2014.2309835.

[33] D.B. Camarillo, C.F. Milne, C.R. Carlson, M.R. Zinn, J.K. Salisbury, Mechanics modeling of tendon-driven continuum manipulators, IEEE Trans. Robot. 24 (2008) 1262–1273, http://dx.doi.org/10.1109/TRO.2008.2002311.

[34] M.M. Dalvand, S. Nahavandi, R.D. Howe, An analytical loading model for n -Tendon continuum robots, IEEE Trans. Robot. 34 (2018) 1215–1225, http://dx.doi.org/10.1109/TRO.2018.2838548.

[35] B. Kim, J. Ryu, K.-J. Cho, Joint angle estimation of a tendon-driven soft wearable robot through a tension and stroke measurement, Sensors 20 (2020) 2852, http://dx.doi.org/10.3390/s20102852.

[36] C. Della Santina, C. Duriez, D. Rus, Model-based control of soft robots: A survey of the state of the art and open challenges, IEEE Control. Syst. 43 (2023) 30–65, http://dx.doi.org/10.1109/MCS.2023.3253419.

[37] J. Duan, K. Zhang, K. Qian, J. Hao, Z. Zhang, C. Shi, An operating stiffness controller for the medical continuum robot based on impedance control, Cyborg. Bionic Syst. 5 (2024) 0110, http://dx.doi.org/10.34133/cbsystems.0110.

[38] V. Falkenhahn, T. Mahl, A. Hildebrandt, R. Neumann, O. Sawodny, Dynamic modeling of bellows-actuated continuum robots using the Euler–Lagrange formalism, IEEE Trans. Robot. 31 (2015) 1483–1496, http://dx.doi.org/10.1109/TRO.2015.2496826.

[39] J.-J.E. Slotine, Weiping Li, On the adaptive control of robot manipulators, Int. J. Robot. Res. 6 (1987) 49–59, http://dx.doi.org/10.1177/027836498700600303.

[40] Z. Li, C.-Y. Su, G. Li, H. Su, Fuzzy approximation-based adaptive backstepping control of an exoskeleton for human upper limbs, IEEE Trans. Fuzzy Syst. 23 (2015) 555–566, http://dx.doi.org/10.1109/TFUZZ.2014.2317511.

[41] L.-X. Wang, J.M. Mendel, Fuzzy basis functions, universal approximation, and orthogonal least-squares learning, IEEE Trans. Neural Netw. 3 (1992) 807–814, http://dx.doi.org/10.1109/72.159070.

[42] J. Li, S. Wang, Z. Zhang, C. Shi, A robotic system for transanal endoscopic microsurgery: Design, dexterity optimization, and prototyping, IEEE Robot. Autom. Mag. (2023) 2–16, http://dx.doi.org/10.1109/MRA.2023.3323849.

[43] Y. Xu, D. Song, Z. Zhang, S. Wang, C. Shi, A novel extensible continuum robot with growing motion capability inspired by plant growth for path-following in transoral laryngeal surgery, Soft Robot. (2023) http://dx.doi.org/10.1089/soro.2023.0014, soro.2023.0014.

[44] L. Wang, C. Zhou, Y. Cao, R. Zhao, K. Xu, Vision-based markerless tracking for continuum surgical instruments in robot-assisted minimally invasive surgery, IEEE Robot. Autom. Lett. 8 (2023) 7202–7209, http://dx.doi.org/10.1109/LRA.2023.3315229.

[45] X. Ma, P.W.-Y. Chiu, Z. Li, Shape sensing of flexible manipulators with visual occlusion based on bezier curve, IEEE Sensors J. 18 (2018) 8133–8142, http://dx.doi.org/10.1109/JSEN.2018.2862925.

[46] A.A. Nazari, K. Zareinia, F. Janabi-Sharifi, Visual servoing of continuum robots: Methods, challenges, and prospects, Robot. Comput. Surg. 18 (2022) e2384, http://dx.doi.org/10.1002/rcs.2384.

[47] W. Ba, X. Dong, A. Mohammad, M. Wang, D. Axinte, A. Norton, Design and validation of a novel fuzzy-logic-based static feedback controller for tendon-driven continuum robots, IEEE/ASME Trans. Mechatron. 26 (2021) 3010–3021, http://dx.doi.org/10.1109/TMECH.2021.3050263.

[48] F. Ma, G. Chen, Modeling large planar deflections of flexible beams in compliant mechanisms using chained beam-constraint-Model1, J. Mech. Robot. 8 (2016) 021018, http://dx.doi.org/10.1115/1.4031028.

[49] Y. Chen, S. Yao, M.Q.-H. Meng, L. Liu, Chained spatial beam constraint model: A general kinetostatic model for tendon-driven continuum robots, IEEE/ASME Trans. Mechatron. 29 (2024) 3534–3545, http://dx.doi.org/10.1109/TMECH.2023.3348510.

[50] C. Shi, Z. Tang, S. Wang, Design and experimental validation of a fiber bragg grating-enabled force sensor with an ortho-planar spring-based flexure for surgical needle insertion, IEEE Trans. Med. Robot. Bionics 3 (2021) 362–371, http://dx.doi.org/10.1109/TMRB.2021.3073198.

[51] Y. Hao, H. Zhang, Z. Zhang, C. Hu, C. Shi, Development of force sensing techniques for robot-assisted laparoscopic surgery: A review, IEEE Trans. Med. Robot. Bionics 6 (2024) 868–887, http://dx.doi.org/10.1109/TMRB.2024.3407238.